Polymer 338 (2025) 129041

Contents lists available at ScienceDirect

Polymer

journal homepage: www.elsevier.com/locate/polymer

Octavinylsilsesquioxane-based Organic–Inorganic hybrid polymers with double-decker silsesquioxane (DDSQ) derivative: Hierarchical structures with enhanced CO_2 and dye adsorption performance

Yang-Chin Kao [a], Pin-Han Chen [a], Cheng-Yu Chen [a], Hui-Wen Chen [a], Wei-Cheng Chen [a], Mohsin Ejaz [a], Mohammed G. Kotp [a], Mohamed Gamal Mohamed [a], Hira Karim [b], Shiao-Wei Kuo [a,c,*]

[a] Department of Materials and Optoelectronic Science, Center of Crystal Research, National Sun Yat-Sen University, Kaohsiung, 804, Taiwan
[b] Department of Chemistry, School of Natural Sciences (SNS), National University of Sciences and Technology (NUST), H-12, Islamabad, 44000, Pakistan
[c] Department of Medicinal and Applied Chemistry, Kaohsiung Medical University, Kaohsiung, 807, Taiwan

ARTICLE INFO

Keywords:
Organic/inorganic hybrid
CO_2 uptake
Dye adsorption

ABSTRACT

In this work, we report the preparation and comprehensive investigation of octavinylsilsesquioxane (OVS)-based porous organic-inorganic polymers (POIPs) derived from bromo-functionalized double-decker silsesquioxane (DDSQ-Br) and 1,4-dibromobenzene (PD-Br) with OVS monomer. The DDSQ-Br monomer was prepared via both the Heck and Grubbs reactions, with detailed analyses performed using Fourier-transform infrared (FT-IR) spectroscopy and nuclear magnetic resonance (NMR) spectroscopy, including ^{1}H, ^{13}C, and ^{29}Si NMR. The FT-IR spectra confirmed the characteristic stretching vibrations of the corresponding monomer derivatives. At the same time, NMR data indicated that the Heck reaction tends to yield DDSQ oligomers, in contrast to the well-resolved signals observed for the monomer produced via the Grubbs reaction. Subsequent polymerization from cubic OVS with DDSQ-Br or 1,4-dibromobenzene resulted in the formation of two distinct POIPs: OVS-DDSQ POIP and OVS-PD POIP. These materials exhibit hierarchical pore structures, as confirmed by N_2 adsorption/desorption isotherms and pore size analyses, with BET surface areas of 692 m^2/g and 407 m^2/g, respectively. Thermogravimetric analysis (TGA) profiles revealed enhanced thermal stability for these POIPs, attributed to their highly crosslinked networks. Moreover, these POIPs demonstrate promising adsorption performance for both CO_2 capture and organic dye removal. At 298 K, the CO_2 uptake capacities of OVS-DDSQ and OVS-PD POIPs were 0.25 and 0.15 mmol/g, respectively, increasing significantly at 273 K to 0.74 and 0.45 mmol/g, respectively. Dye adsorption studies using Rhodamine B (RhB) showed rapid decolorization, with kinetic analyses indicating that the adsorption process in OVS-DDSQ POIP is predominantly governed by pseudo-first-order kinetics, while OVS-PD POIP fits both kinetic models well. The superior performance of OVS-DDSQ POIP is ascribed to its enhanced surface area, abundant micropores, and rich phenyl content, which promote stronger polar-π interactions with CO_2 and dye molecules.

1. Introduction

Over the past few decades, the textile industry has rapidly expanded and become a cornerstone of modern economies. However, this growth has also introduced significant environmental challenges [1–6]. The extensive use of organic dyes, crucial for producing vibrant textile colors, has resulted in severe wastewater pollution. These dyes are not only visually unappealing but also toxic, persistent, and potentially carcinogenic, posing serious risks to aquatic ecosystems and human health. Furthermore, the energy-intensive nature of textile production contributes substantially to greenhouse gas emissions, particularly carbon dioxide, which exacerbates global warming and underscores the urgent need for sustainable industrial practices. In response to these challenges, researchers are developing innovative materials that can

* Corresponding author. Department of Materials and Optoelectronic Science, Center of Crystal Research, National Sun Yat-Sen University, Kaohsiung, 804, Taiwan.
E-mail address: kuosw@faculty.nsysu.edu.tw (S.-W. Kuo).

https://doi.org/10.1016/j.polymer.2025.129041
Received 14 April 2025; Received in revised form 22 August 2025; Accepted 6 September 2025
Available online 8 September 2025

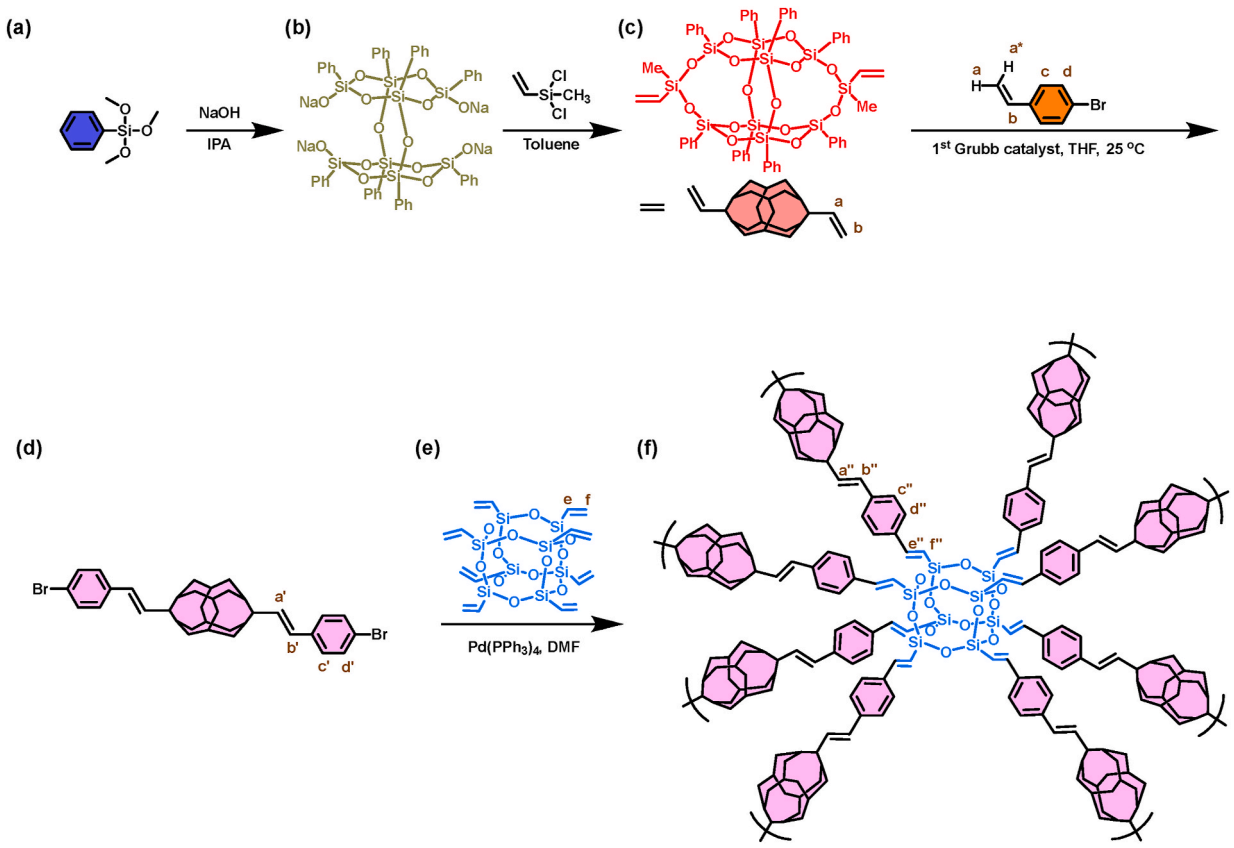

Scheme 1. The preparation of (d) dibromo-functionalized DDSQ cage (DDSQ-Br) from (a) phenyltrimethoxylsilane, (b) DD-Na, and (c) DDSQ-Vinyl compounds, followed by a Heck reaction with (e) OVS to obtain (f) OVS-DDSQ POIP.

efficiently adsorb both CO_2 and organic dyes [7,8]. Traditional adsorbents like activated carbon and natural zeolites have been widely used due to their high adsorption capacities and unique crystalline structures. However, despite the high effectiveness of activated carbon and the structural versatility of zeolites, their ability to address the full range of adsorption needs in modern industrial processes remains limited. Moreover, the environmental impact of synthetic dyes extends beyond the textile industry to sectors such as leather and food processing, where these dyes are also prevalent. The discharge of dye-contaminated wastewater disrupts the photosynthetic processes of aquatic plants, threatens aquatic life, and increases the risk of cancer in humans [9–13]. Therefore, it is critical to treat dye-laden wastewater before its discharge into the environment. Diverse methodologies have been implemented to address this issue, including membrane filtration, chemical oxidation, photodegradation, and biological approaches. Among these, adsorption has emerged as a promising and cost-effective method, owing to its high efficiency, operational simplicity, economic feasibility, and potential for regeneration [12–15].

Rhodamine B (RhB), a commonly used dye, finds broad applications in industries such as food, textiles, and leather processing. Despite its broad application, RhB is highly toxic and has been linked to carcinogenic and mutagenic effects, posing a serious threat to various life forms [16–21]. Its long-lasting impact on aquatic ecosystems is particularly alarming, as RhB hinders light penetration, thereby hindering photosynthetic activity and interfering with natural self-purification mechanisms, RhB poses a significant ecological threat. Therefore, its complete elimination from industrial effluents is crucial to minimizing adverse environmental impacts. To address this, a range of conventional techniques has been utilized, such as membrane filtration, sedimentation, coagulation, adsorption, and photodegradation. In the adsorption process, the nature and characteristics of the adsorbent are key determinants of the adsorption efficiency of dye removal from aqueous solutions. As a result, developing new adsorbents is key to enhancing the effectiveness of this method.

Recently, there has been significant interest in hybrid materials composed of inorganic and organic constituents that leverage the strengths of both, achieved by incorporating inorganic entities into an organic matrix [22,23]. Poly(silsesquioxanes), represented by the formula $(RSiO_{1.5})_n$, serve as foundational building blocks or scaffolds in creating these hybrid materials. By adjusting polymerization conditions, these compounds can form various structures, such as cages, ladder polymers, and nanoparticles [24–32]. A typical example is polyhedral oligomeric silsesquioxane (POSS), which features a well-defined cubic (T_8) architecture with the molecular formula $R_8Si_8O_{12}$. This structure consists of an inorganic Si_8O_{12} core functionalized at each of its eight corners with organic substituents (R groups). The rigid siloxane framework imparts exceptional thermal and chemical stability and enables the formation of highly symmetrical architecture, star-shaped structures. These unique features distinguish them significantly from planar molecules, making rigid polyhedral structures highly attractive as building blocks for tailored molecular entities and materials at the nanoscale [33–38].

In our previous studies, we conducted an in-depth analysis of the various structural configurations present in polymer/POSS hybrid systems, demonstrating that these configurations are significantly influenced by the specific functionalization of POSS derivatives [39–41]. One derivative that has garnered considerable attention is double-decker silsesquioxane (DDSQ), a distinctive class of organic/inorganic hybrid compounds. DDSQ integrates the exceptional thermal stability and structural rigidity inherent to its inorganic framework with the reactivity and versatility provided by its organic functional groups [42–48]. This unique combination of properties renders DDSQ an excellent candidate for enhancing the overall thermal and chemical stability of main-chain polymer/DDSQ hybrids [49–51]. By incorporating DDSQ

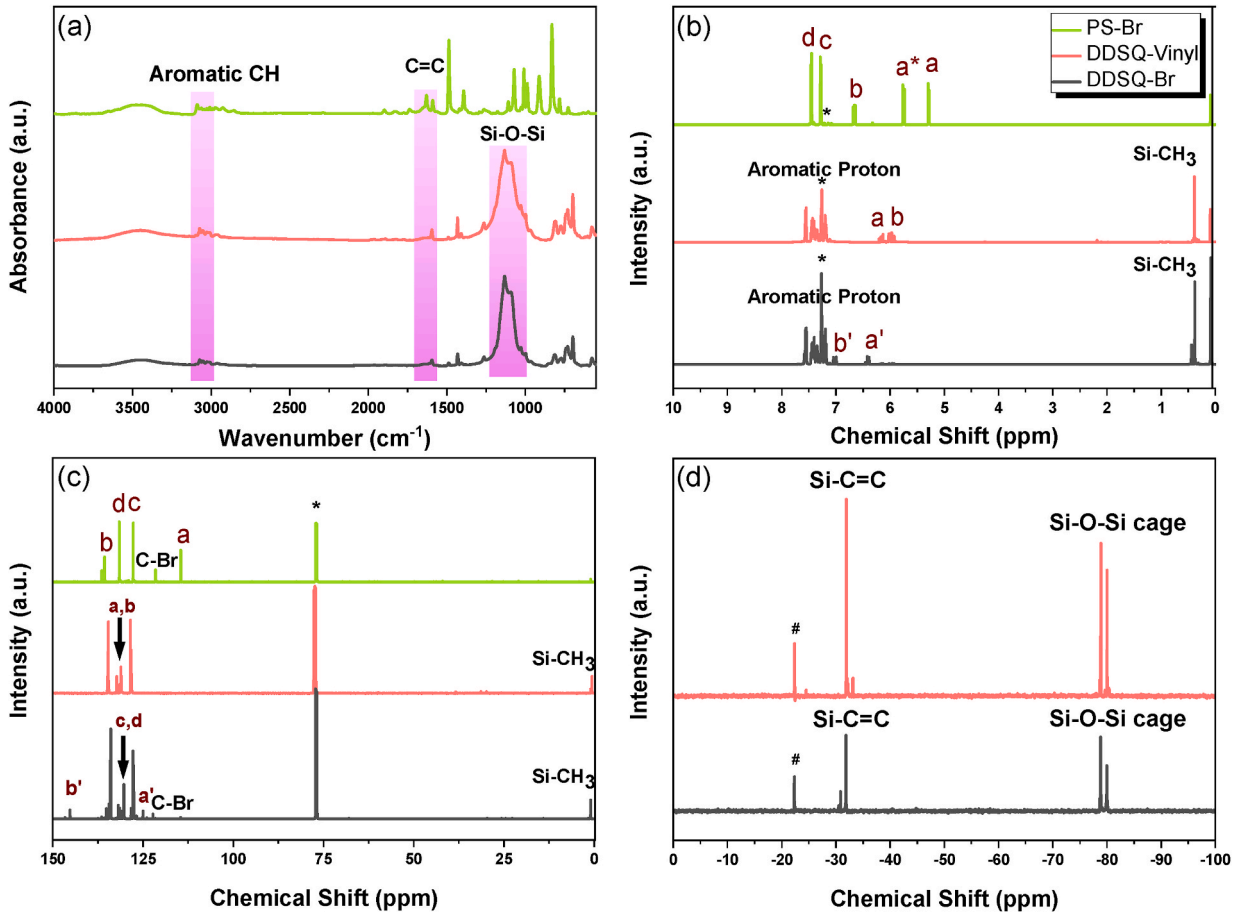

Fig. 1. (a) FT-IR spectra, (b) ^{1}H NMR spectra, (c) ^{13}C NMR spectra, and (d) ^{29}Si NMR of PS-Br (* is the peak for Chloroform-*d*), DDSQ-Vinyl, and DDSQ-Br ($^{\#}$ is the peak for long chain aliphatic-Si-O).

into the polymer backbone, it is possible to create advanced materials that not only withstand high temperatures and harsh chemical environments but also exhibit improved mechanical performance. These enhanced characteristics open new avenues for the development of robust materials suited for broad applicability in industrial and technological fields.

Recent efforts have demonstrated the promise of POSS as a building block for porous materials; however, few studies systematically compare how different coupling strategies, or the incorporation of large organosilicon cages, influence microstructure and performance. In this work, we report the synthesis of a difunctional brominated DDSQ monomer (DDSQ-Br) and a direct comparison of two coupling routes—Heck and Grubbs [52–59]. Using ^{1}H, ^{13}C, and ^{29}Si NMR and FT-IR spectroscopy, we show that the Heck reaction between DDSQ and 1,4-dibromobenzene (PD-Br) tends to induce continuous coupling and self-polymerization, producing oligomeric/long-chain DDSQ species. In contrast, the Grubbs reaction between DDSQ and 4-bromostyrene selectively yields a monomeric DDSQ-Br species without promoting self-polymerization. The different reaction outcomes are reflected in the NMR spectra: Heck-derived samples exhibit broadened signals consistent with oligomerization. At the same time, Grubbs-derived DDSQ-Br displays well-resolved splitting patterns indicative of preserved monomeric structure. The DDSQ-Br monomer was subsequently integrated with octavinyl-POSS (OVS) via Heck coupling to produce an OVS-DDSQ POIP. For comparison, OVS was also coupled with PD-Br under analogous conditions to form an OVS-PD POIP. Both hybrid networks were thoroughly characterized by FT-IR, liquid- and solid-state ^{29}Si NMR, TGA, N_2 adsorption/desorption (BET and pore size analyses), SEM/-TEM, and XPS. The OVS-DDSQ POIP exhibits hierarchical micro/mesoporosity and a high BET surface area (OVS-DDSQ POIP: 692 m^2/g vs OVS-PD POIP: 407 m^2/g), distinct micropore peaks (1.0 nm for OVS-DDSQ POIP; 1.8 nm for OVS-PD POIP), and markedly improved thermal stability (T_{d10} and char yield values consistent with a highly crosslinked Si-O-Si/benzene network). These structural features translate into superior functional performance: OVS-DDSQ POIP shows enhanced CO_2 uptake (e.g., 0.25 mmol/g at 298 K and 0.74 mmol/g at 273 K) and faster, higher-capacity RhB removal compared with the OVS-PD POIP. Mechanistically, the improved adsorption behavior of OVS-DDSQ POIP is attributed to the combined effects of abundant micropores. These Si-O-Si cage sites serve as active adsorption loci, and rich phenyl content within the DDSQ unit that promotes polar-π/π-π and chemisorptive interactions with guest molecules. More broadly, this study demonstrates a practical design strategy for tuning the microstructure and adsorption function of POSS-based hybrid materials by selecting appropriate coupling chemistries and by introducing large organosilicon cages such as DDSQ.

2. Experimental section

2.1. Materials

Octavinylsilsesquioxane (OVS, 97 %) and $Pd(PPh_3)_4$ (98 %) were obtained from Leyan. Phenyltrimethoxysilane (97 %) and trimethoxy (phenyl)silane (97 %) were purchased from Sigma-Aldrich, while 1,4-dibromobenzene (PD-Br, 98 %), toluene (99 %), and dichloro(methyl) (vinyl)silane (97 %) were supplied by Alfa Aesar. *N*, *N*-Dimethylformamide (DMF) was sourced from DUKSAN. Potassium carbonate (K_2CO_3, 99 %) and sodium hydroxide (NaOH, 97 %) were acquired from

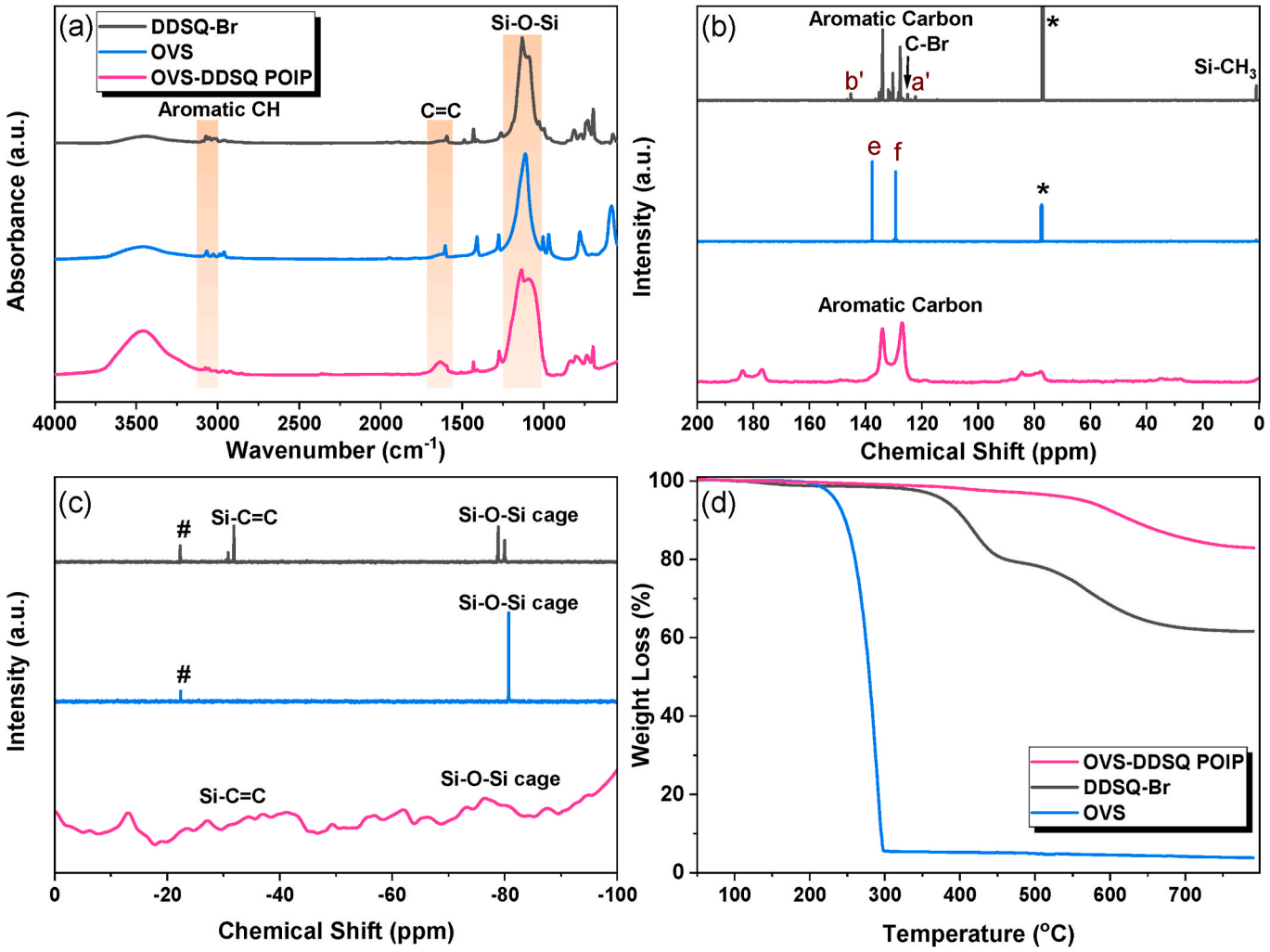

Fig. 2. (a) FT-IR spectra, (b) ^{13}C NMR spectra (* is the peak for Chloroform-*d*), (c) ^{29}Si NMR spectra ($^{\#}$ is the peak for long chain aliphatic-Si-O), and (d) TGA profiles of OVS, DDSQ-Br, and OVS-DDSQ.

SHOWA. Isopropanol (IPA), tetrahydrofuran (THF), *N*, *N*-diethylethanamine (Et_3N), and hexane were purchased from Merck. Additionally, 4-bromostyrene (PS-Br, 95 %) and benzylidene-bis (tricyclohexylphosphino)-dichlororuthenium (96 %), which is the first-generation Grubbs catalyst, were obtained from Combi-Block. Dichloromethane (DCM, 99 %) was purchased from Thermo Scientific. Additionally, in our previous research [32,60,61], the synthesis of DD-Na was successfully achieved, as illustrated in Scheme 1(b).

2.2. Synthesis of bis-vinyl double-decker silsesquioxane (DDSQ-vinyl) [62]

DD-Na (1.00 g, 0.86 mmol), dichloro(methyl) (vinyl)silane (0.35 mL, 2.69 mmol), Et_3N (0.1 mL), and 50 mL toluene were added to a reaction flask and maintained the reaction for 6 h with stirring at 0 °C, as shown in Scheme 1(c). Followed by an additional 6 h of stirring at 25 °C., the solution was filtered, and the filtrate was extracted with DCM, yielding white solid products with a yield of 66 %.

2.3. Synthesis of bis-bromo double-decker silsesquioxane (DDSQ-Br)

DDSQ-Vinyl (0.70 g, 0.58 mmol), PS-Br (0.33 mL, 2.55 mmol), the 1st generation Grubbs catalyst (60 mg), and 50 mL THF were added to a reaction flask and stirred under N_2 for 2 days as [Scheme 1(d)]. Following the completion of the reaction, the mixture was subjected to filtration, after which 500 mL of chilled hexane was introduced to the filtrate to promote pale-yellow precipitation [Yield: 43 %].

2.4. Synthesis of OVS-DDSQ POIP

DDSQ-Br (0.20 g, 0.13 mmol), OVS (0.02 g, 0.03 mmol), $Pd(PPh_3)_4$ (50 mg), K_2CO_3 (0.09 g, 0.66 mmol), and 60 mL DMF. The reaction mixture was maintained under continuous stirring at 120 °C in an inert N_2 for 72 h. The mixture was filtered to remove solid impurities. The residue was washed thoroughly with THF and dried in a vacuum oven at 60 °C for one day, yielding a gray solid.

2.5. Synthesis of OVS-PD POIP

To the reaction flask, K_2CO_3 (0.77 g, 5.50 mmol), OVS (0.35 g, 0.56 mmol), $Pd(PPh_3)_4$ (88 mg), 30 mL DMF and PD-Br (0.53 g, 2.21 mmol) were added, and the reaction mixture was maintained under continuous stirring at 120 °C in an inert N_2 for 72 h. The resulting solid was washed with H_2O, DMF, and THF, respectively, to produce OVS-PD POIP as a white powder.

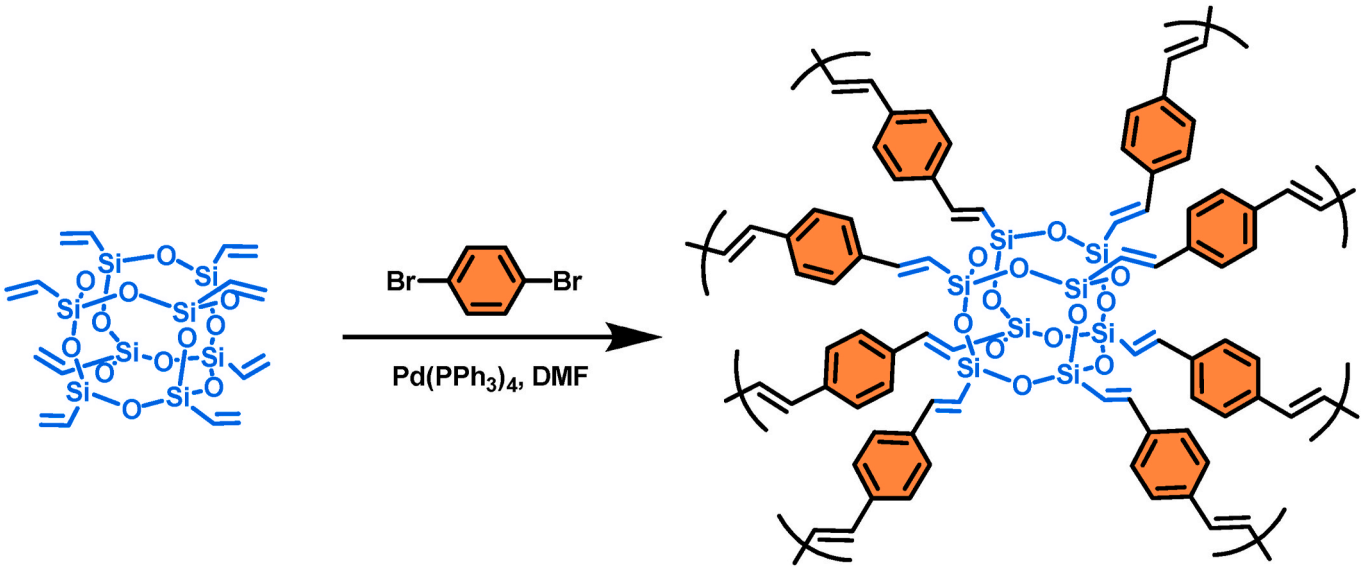

Scheme 2. The preparation of OVS-PD POIP from OVS.

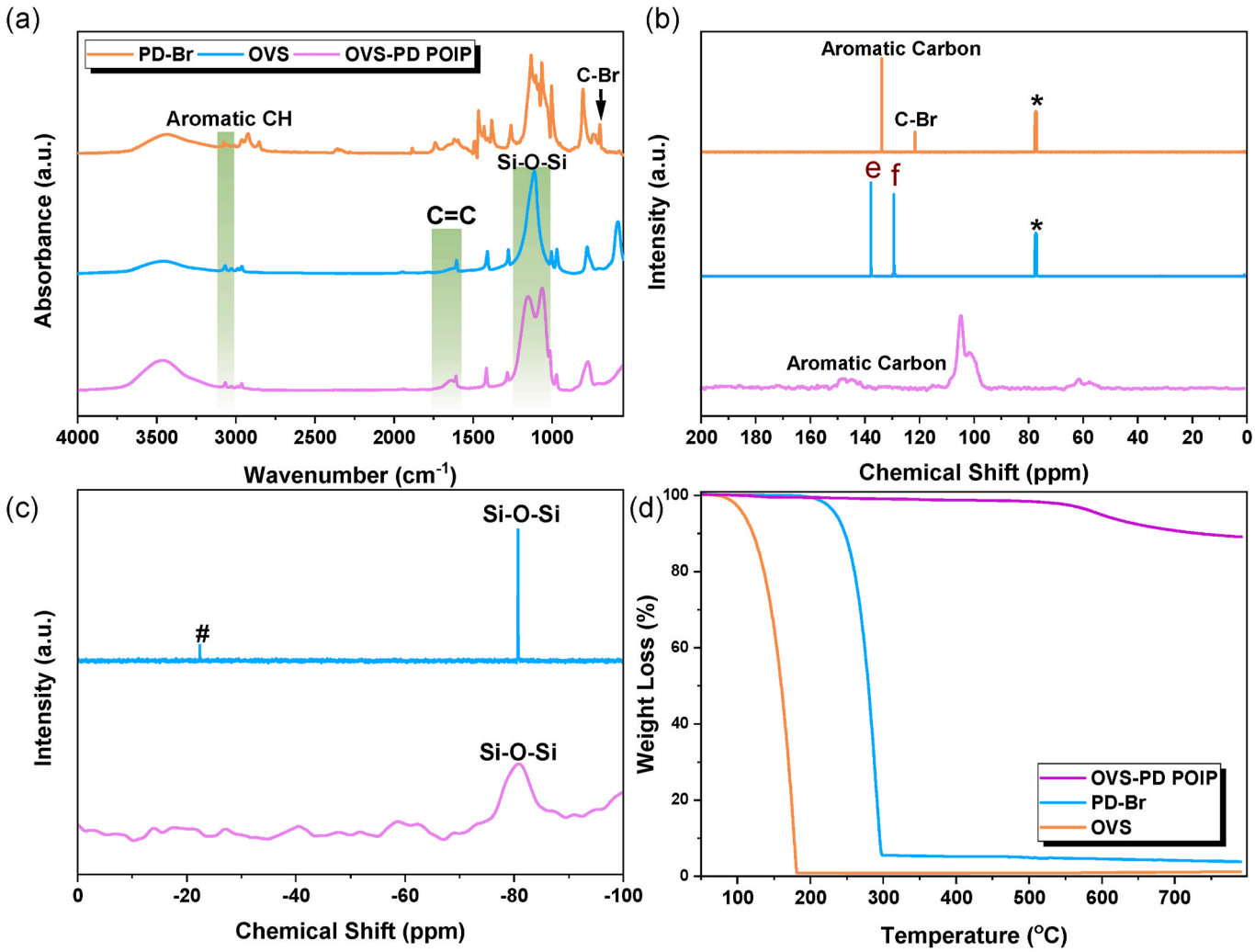

Fig. 3. (a) FT-IR spectra, (b) ^{13}C NMR spectra (* is the peak for Chloroform-*d*), (c) ^{29}Si NMR spectra ($^{\#}$ is the peak for long chain aliphatic-Si-O), and (d) TGA analysis of PD-Br, OVS, and OVS-PD POIPs.

3. Results and discussion

3.1. Synthesis and characterization of DDSQ-Br monomer

The FT-IR spectra are illustrated in Fig. 1(a) for each monomer derivative during the preparation of DDSQ-Br. The FTIR spectrum of PS-Br exhibits sp^2 C-H stretching at 3089 cm^{-1} and a C═C stretching corresponding to the substituents on the benzene ring at 1629 cm^{-1}. For the DDSQ derivative, strong absorption peaks attributed to two organosilicon groups appear at 1262 cm^{-1} (Si-CH_3 units) and 1133 cm^{-1} (Si-O-Si units), while the aromatic ring absorption is observed at 3073 cm^{-1} [60,61]. Additionally, all derivatives display a characteristic C═C stretching absorption at 1595 cm^{-1}. Due to the relatively large size of the DDSQ structure, subtle spectral changes in FT-IR are difficult to detect. However, structural modifications can be more effectively analyzed using NMR spectroscopy. Fig. 1(b) reveals the ^{1}H NMR spectra of PS-Br, DDSQ-Vinyl, and DDSQ-Br. In the PS-Br spectrum, the aromatic protons appear at 7.28–7.44 ppm. The Ar-C**H**═CH_2 signals are observed at 6.63–6.68 ppm (peak *b*, doublets of doublets), and the Ar-CH═C**H_2** signals are detected at 5.73–5.76 ppm and 5.27–5.29 ppm (peak *a*, doublets of doublets). The DDSQ-Vinyl spectrum exhibits aromatic proton signals at 7.18–7.56 ppm, Si-C**H**═CH_2 peaks at 6.13–6.20 ppm (peak *a*, doublets of doublets), and Si-CH═C**H_2** peaks at 5.92–6.03 ppm (peak *b*, doublets of doublets), along with a Si-CH_3 signal at 0.39 ppm. For DDSQ-Br, two different reaction methods were employed. When prepared by the Heck reaction with excess PD-Br [Scheme S1], the spectrum shows aromatic protons at 7.08–7.58 ppm; nevertheless, the aromatic ring signal is broad. In addition, the Si-C**H**═CH signals are observed at 6.37–6.42 ppm (peak *a'*), and Si-CH═C**H** signals are detected at 6.89–6.97 ppm (peak *b'*), with a Si-CH_3 signal at 0.43 ppm [Fig. S1]. In contrast, when DDSQ-Br is prepared by the Grubbs reaction with PS-Br, aromatic protons emerge at 7.18–7.54 ppm with a clearly defined aromatic signal. The Si-CH═CH signals are observed at 6.38–6.42 ppm (peak *a'*) and 6.99–7.04 ppm (peak *b'*), along with a Si-CH_3 signal at 0.38 ppm. Fig. 1(c) displays the ^{13}C NMR spectra of PS-Br, DDSQ-Vinyl, and DDSQ-Br. In the PS-Br spectrum, the aromatic carbons appear in the range of 121–136 ppm, with aromatic C-Br signals clearly evident at 121 ppm, and Ar-C═C signals appearing at 114 and 135 ppm. The DDSQ-Vinyl spectrum shows aromatic carbon signals at 128–135 ppm, Si-C═C peaks at 131–132 ppm, and a Si-CH_3 signal at 0.61 ppm.

For DDSQ-Br prepared by the Heck reaction, the aromatic carbons appear at 122–134 ppm with aromatic C-Br labels at 123 ppm, while Si-C═C signals are observed at 125 and 146 ppm, accompanied by a Si-CH_3 signal at 1.01 ppm [Fig. S2]. When considering DDSQ-Br produced via the Grubbs reaction, the aromatic carbons also appear at 122–134 ppm (with C-Br signals at 122 ppm), and Si-C═C signals are seen at 125 and 145 ppm, along with a Si-CH_3 signal at 1.01 ppm. Due to the similarities in the ^{13}C NMR spectra of DDSQ-Br obtained by either reaction method, the analysis was extended to ^{29}Si NMR spectroscopy, as shown in Fig. 1 (d) and Fig. S3. In the ^{29}Si NMR spectrum of DDSQ-Vinyl, the O_2-Si-CH_3(CH═CH_2) resonance is observed at −31.91 and −33.17 ppm, and

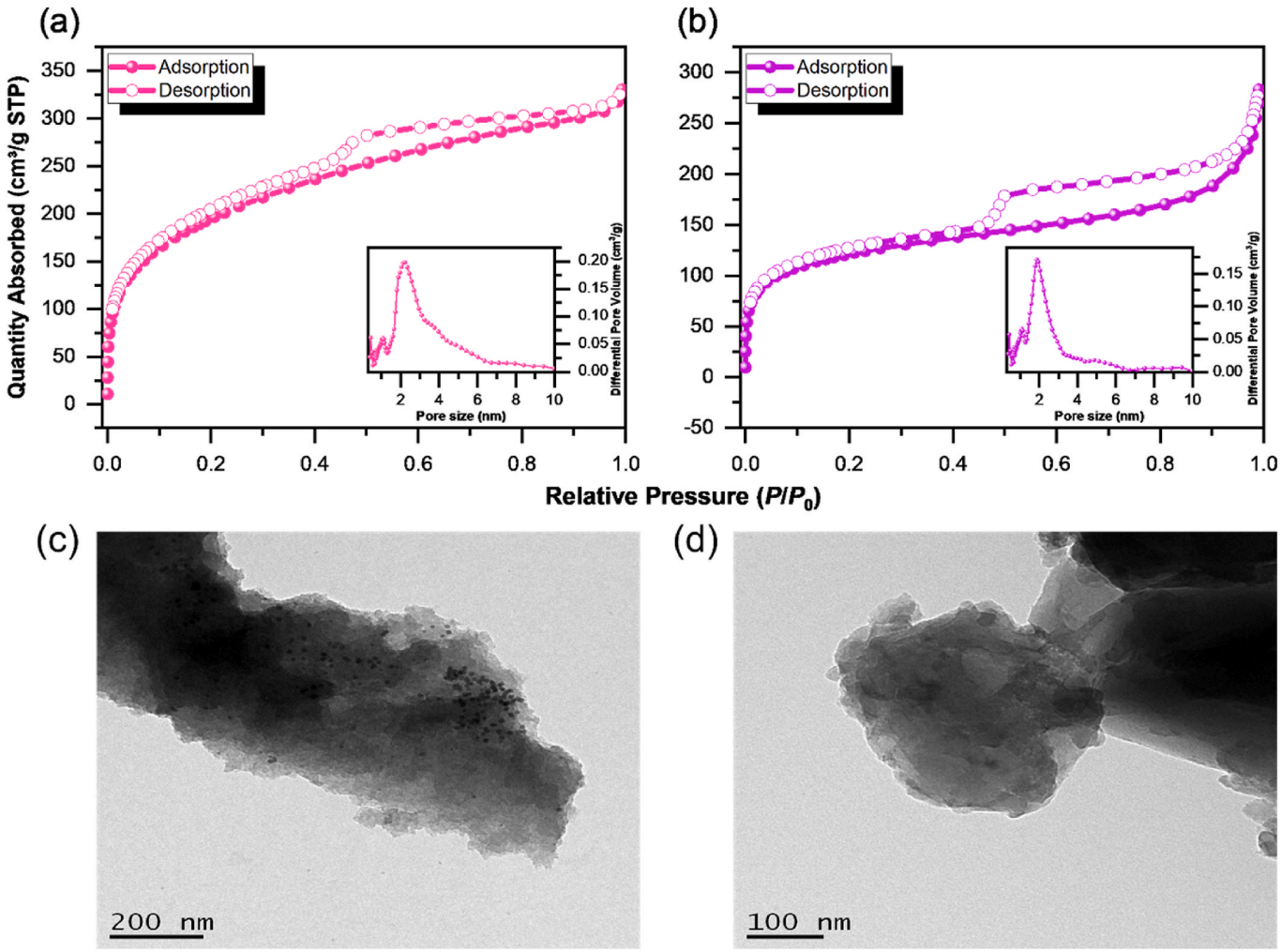

Fig. 4. N_2 adsorption/desorption isotherms and pore size patterns of the (a) OVS-DDSQ POIP and (b) OVS-PD POIP. The corresponding TEM images of (c) OVS-DDSQ and (d) OVS-PD POIPs.

the Si-O-Si cage signals are detected at −78.87 and −80.03 ppm, indicating varied chemical environments around the silicon atoms. After the Heck reaction, the ^{29}Si NMR spectrum shows the O_2-Si-CH_3(CH═CH_2) resonance at −31.00 ppm, while the Si-O-Si cage signals appear as a broad peak between −78 and −81 ppm. Conversely, when the Grubbs reaction is used, the O_2-Si-CH_3(═CH_2) resonance is observed at −30.85 and −31.86 ppm, with the Si-O-Si cage signals clearly detected at −78.84 and −80.00 ppm. Finally, both DDSQ-Vinyl and DDSQ-Br show additional peaks at −22.31 and −22.39 ppm, respectively, which can be assigned to long-chain aliphatic-Si-O species [63]. Based on these NMR results, it can be inferred that the Heck reaction tends to promote the formation of DDSQ oligomers or polymers, as evidenced by the broad signals in both the ^{1}H and ^{29}Si NMR spectra. In contrast, the Grubbs reaction yields a DDSQ-Br monomer, where the splitting patterns in the ^{1}H and ^{29}Si NMR spectra are well resolved. The possible mechanism for the Heck reaction is illustrated in Scheme S2, whereas Scheme S3 shows the mechanism for the Grubbs reaction. Notably, the Grubbs reaction minimizes self-condensation of DDSQ, likely due to steric effects.

3.2. Synthesis and detailed structural investigation of OVS-DDSQ POIP and OVS-PD POIP frameworks

Fig. 2(a) reveals the FT-IR spectra of DDSQ-Br, OVS, and OVS-DDSQ POIP. The spectrum of DDSQ-Br is described in Fig. 1. For OVS, the sp^2 C-H stretching vibration manifests at 3068 cm^{-1}. Its characteristic bands include a C═C stretching of the substituents on the benzene ring at 1629 cm^{-1} and a Si-CH_3 stretching vibration at 1277 cm^{-1}. Moreover, the prominent absorption signals at 1112 cm^{-1} are attributed to Si-O-Si units. After the Heck reaction to obtain OVS-DDSQ POIP, a broader peak is observed between 975 and 1251 cm^{-1}, which is a consequence of the plentiful Si-O-Si units. The Si-CH or Si-CH_3 stretching vibration appears at 1275 cm^{-1}, and the characteristic broad C═C stretching absorption is observed at 1632 cm^{-1}. Fig. 2(b) presents their corresponding ^{13}C NMR spectra. In the OVS spectrum, the signals at 129 ppm and 137 ppm are assigned to Si-CH═CH_2 groups. After the Heck reaction with DDSQ-Br to form OVS-DDSQ POIP, solid-state ^{13}C NMR spectra reveal that the signals at 126.9 and 133.8 ppm can be attributed to phenyl carbons and alkene.

Carbons, with contributions overlapping between OVS and DDSQ-Br. Furthermore, Fig. 2(c) illustrates the ^{29}Si NMR spectra, which reveal distinct differences between OVS and OVS-DDSQ POIP. In the OVS spectrum, a sharp peak at −80.70 ppm corresponds to the Si-O-Si units. After the Heck reaction, the solid-state ^{29}Si NMR spectrum of OVS-DDSQ POIP shows a resonance at approximately −27 ppm for Si-alkene units and another at around −80 ppm for Si-O-Si units, confirming the formation of the OVS-DDSQ POIP network. Fig. 2(d) unveils the TGA curves adopted to investigate the thermal stability of DDSQ-Br, OVS, and OVS-DDSQ POPI under a nitrogen atmosphere. With a heating rate of 20 °C/min up to 800 °C, the T_{d10} values (temperature at 10 % weight loss) are 407 °C for DDSQ-Br, 247 °C for OVS, and 629 °C for OVS-DDSQ POIP, respectively. Additionally, the char yields were 61 %, 3 %, and 83 % for DDSQ-Br, OVS, and OVS-DDSQ POIP, respectively. This result

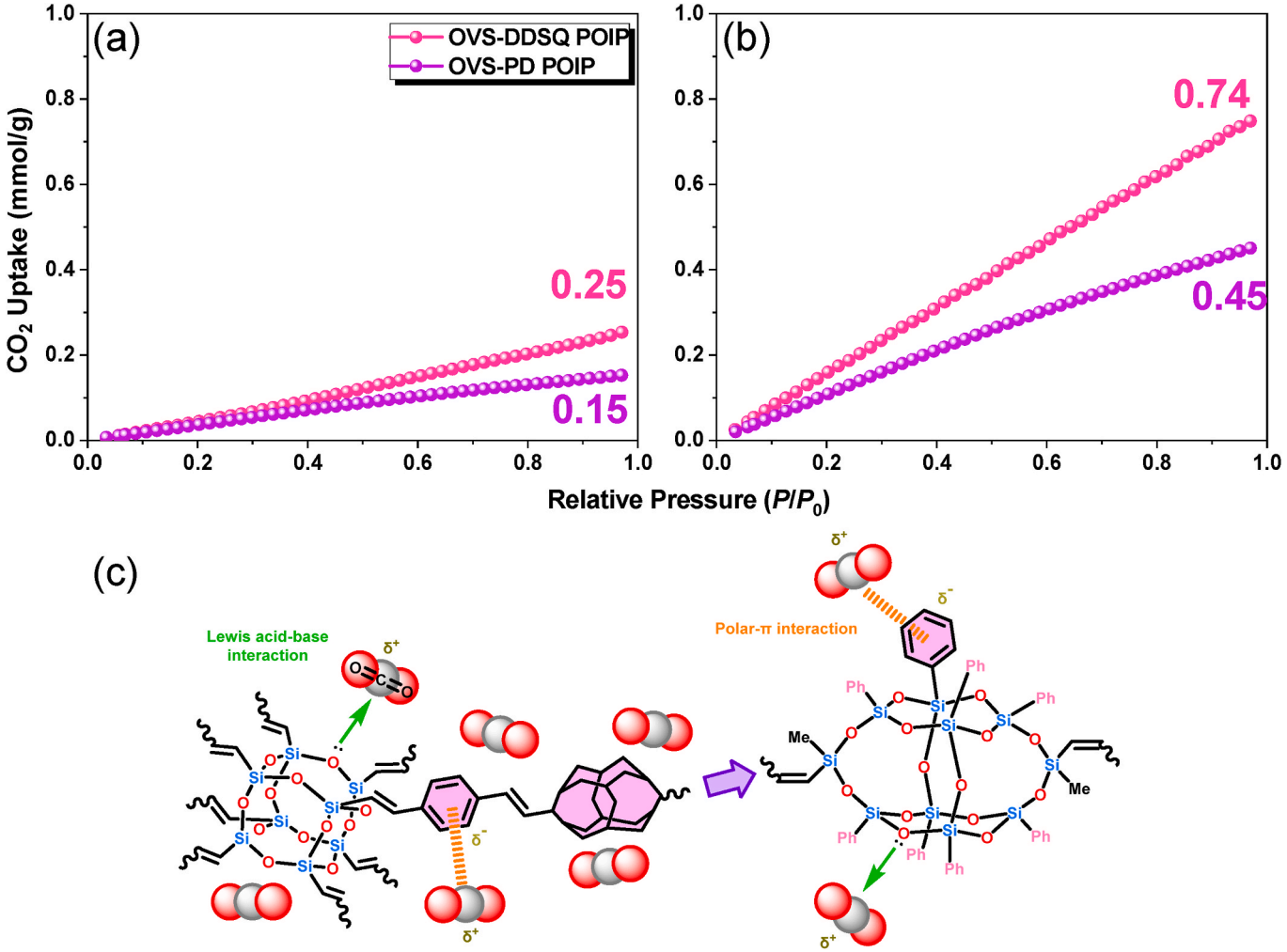

Fig. 5. CO_2 uptake at (a) 298 K and (b) 273 K of OVS-DDSQ POIP and OVS-PD POIP, and (c) possible CO_2 capture mechanisms of OVS-based POIPs.

indicates that OVS-DDSQ POIP demonstrates higher thermal stability compared to DDSQ-Br and OVS, which can be attributed to its highly crosslinked structure formed by the Si-O-Si cage and benzene ring.

OVS-PD POIP was synthesized as a white solid via a Heck coupling reaction between OVS and PD-Br, catalyzed by $Pd(PPh_3)_4$ in the presence of a base, as depicted in Scheme 2.

Fig. 3(a) displays the FT-IR spectra of PD-Br and OVS derivatives. The spectrum of OVS is as mentioned in Fig. 2. In the spectrum of PD-Br, a C-Br signal is observed at 698 cm^{-1}, along with sp^2 C-H stretching at 3077 cm^{-1}. After the Heck reaction with OVS to produce OVS-PD POIP, the resulting spectrum shows a broad absorption peak around 1603 cm^{-1}, associated with the alkene group (C═C), and sp^2 C-H stretching appears at 3065 cm^{-1}. Fig. 3(b) presents the ^{13}C NMR spectra. In the PD-Br spectrum, the aromatic C-Br group is evident at 121 ppm, and another aromatic carbon signal is observed at 133 ppm. After the Heck reaction, the solid-state ^{13}C NMR spectrum of OVS-PD POIP shows sp^2 carbon resonances in the range of 139–152 ppm, confirming the incorporation of alkene groups. Furthermore, Fig. 3(c) illustrates the ^{29}Si NMR spectrum of OVS-PD POIP. A broad peak around −80 ppm, corresponding to Si-O-Si units, confirms the successful synthesis of the OVS-PD POIP network. Additionally, OVS shows a peak at −22.37 ppm, consistent with the signals observed for the DDSQ derivatives (−22.31 and −22.39 ppm), which we attribute to long-chain aliphatic-Si-O species. Finally, Fig. 3(d) presents the TGA results for PD-Br, OVS, and the OVS-PD POIP. The T_{d10} values are 121 °C for PD-Br, 247 °C for OVS, and 734 °C for OVS-PD POIP, while the corresponding char yields are 1 %, 3 %, and 89 %, respectively. These results indicate that OVS-PD POIP exhibits significantly enhanced thermal stability, which can be attributed to its highly crosslinked structure formed between the OVS and PD-Br.

The surface topology and porosity of OVS-based POIPs were analyzed using N_2 adsorption/desorption isotherms. As shown in Fig. 4 (a) and (b), all OVS-based POIPs exhibited type IV isotherms with desorption hysteresis loops, indicating the coexistence of both microporous and mesoporous features. Based on the Brunauer–Emmett–Teller (BET) model, the specific surface areas of OVS-DDSQ and OVS-PD POIPs were calculated to be 692 m^2/g and 407 m^2/g, respectively. The pore size distribution and pore volume were further examined using non-local density functional theory (NLDFT). The analysis substantiated the existence of well-defined microporous structures, with predominant pore sizes of 1.0 nm for OVS-DDSQ POIP and 1.8 nm for OVS-PD POIP.

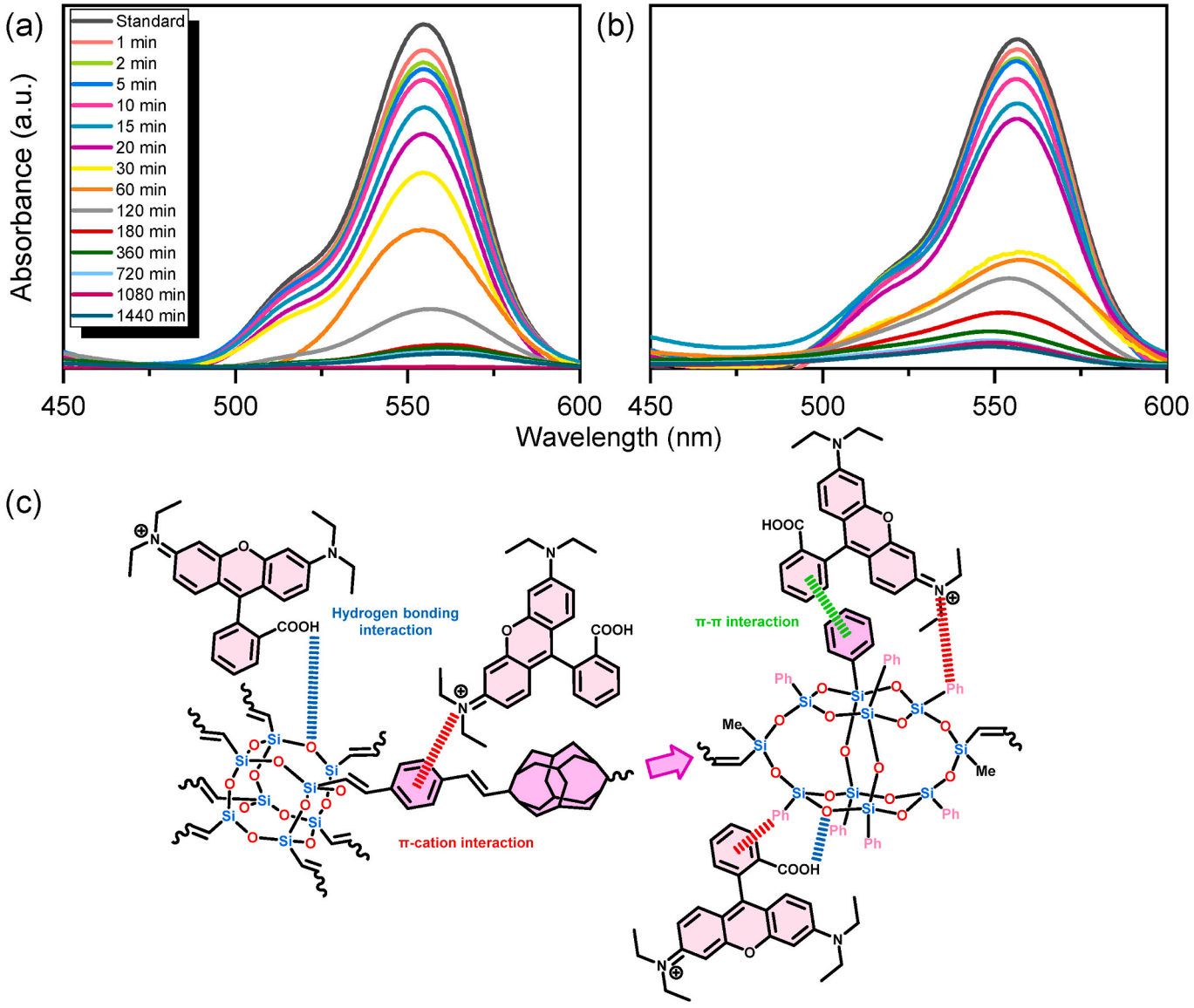

Fig. 6. UV–Vis spectra of (a) OVS-DDSQ and (b) OVS-PD POIPs in aqueous RhB solution at different times; and (c) possible RhB adsorption mechanisms of OVS-based POIPs.

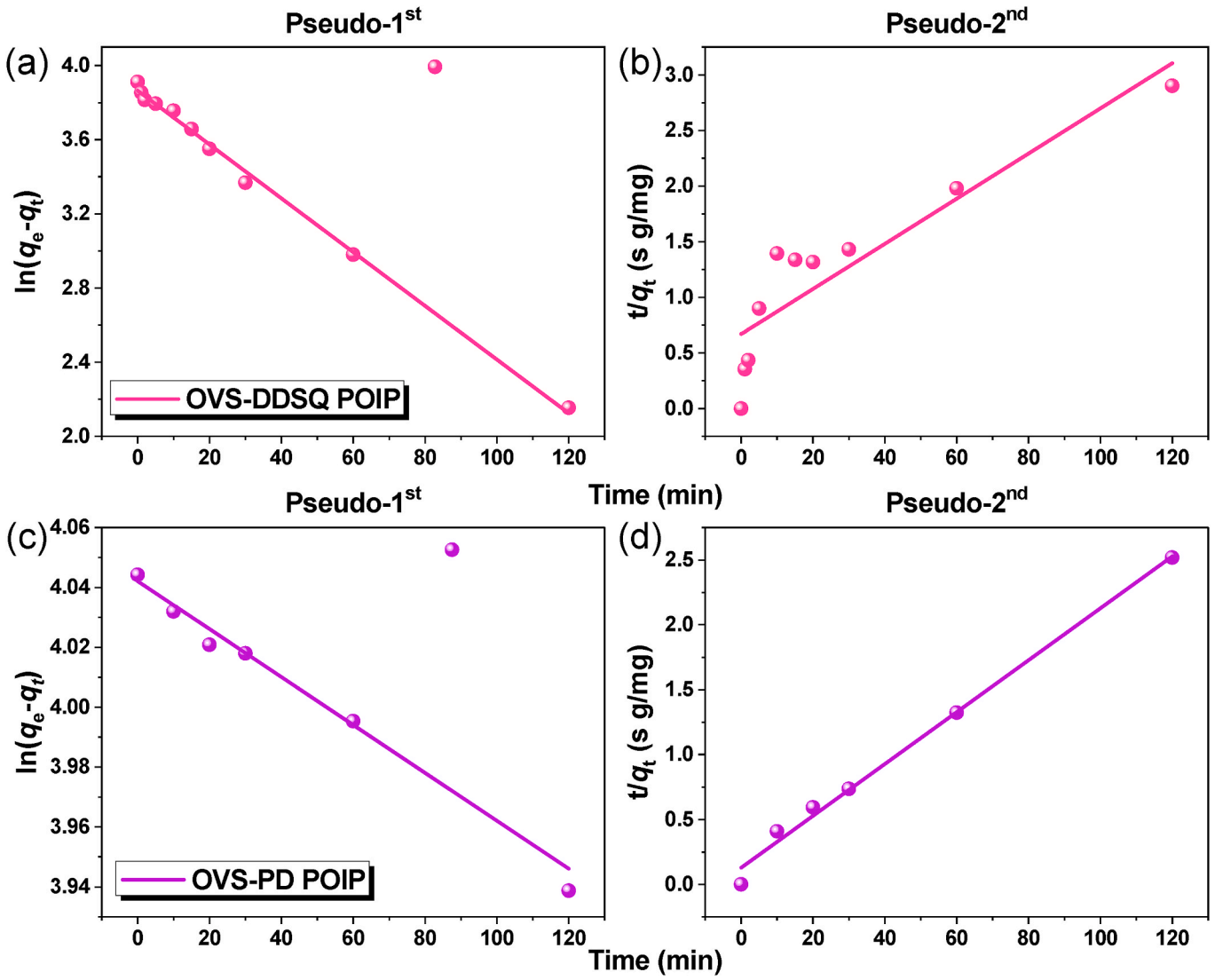

Fig. 7. Pseudo-first-order kinetic fitting of (a) OVS-DDSQ POIP and (c) OVS-PD POIP. Pseudo-second-order kinetic fitting of (b) OVS-DDSQ POIP and (d) OVS-PD POIP.

In addition, mesoporous structures were identified, with dominant pore sizes of 2.1 nm and 4.8 nm for OVS-DDSQ POIP and OVS-PD POIP, respectively. These findings underscore the hierarchical porosity of OVS-based POIPs, which could be advantageous for applications requiring both microporosity and mesoporosity. Moreover, Fig. 4(c) reports a TEM image that OVS-DDSQ POIP tends to form agglomerates, while Fig. 4(d) shows a TEM image, revealing that OVS-PD POIP displays a uniform morphology.

3.3. Adsorption performance analyses of OVS-DDSQ POIP and OVS-PD POIP

The OVS-based POIPs exhibit promising CO_2 adsorption performance, primarily due to their high specific surface areas, abundant micropores, and the presence of Si-O-Si units that act as active sites for CO_2 capture. Under conditions of 298 K and 1 bar, the CO_2 adsorption capacities of OVS-DDSQ and OVS-PD POIPs were measured at 0.25 and 0.15 mmol/g, respectively. When the temperature decreased to 273 K, the adsorption capacities significantly increased to 0.74 mmol/g for OVS-DDSQ POIP and 0.45 mmol/g for OVS-PD POIP, as depicted in Fig. 5(a) and (b). This superior CO_2 adsorption capacity of OVS-DDSQ POIP can be attributed to the presence of the DDSQ structure, which enhances polar-π interactions between the benzene rings and CO_2 molecules, as illustrated in Fig. 5(c).

In addition to CO_2 capture, these OVS-based POIPs demonstrate excellent efficiency in removing organic dyes, making them promising materials for mitigating both air and water pollution. The adsorption process is driven by multiple interactions, including Lewis acid–base interactions, hydrogen bonding, and π–π interactions between the dye molecules and the adsorbent, all of which enhance the physical and chemical attachment of the dyes. To evaluate the dye adsorption capacity of OVS-DDSQ, experiments were conducted using RhB solutions following a previously established procedure [37]. The concentration of RhB was monitored via UV–Vis spectroscopy by recording the absorbance at 555 nm over a period of 0–1440 min, with periodic filtration to separate the suspension. After 5 mg of the adsorbent was mixed with 10 mL of a 25 mg/L RhB solution, the pink dye solution was nearly decolorized to a light pink hue within 30 min. As shown in Fig. 6, the gradual decrease in UV–Vis absorption intensity confirmed the continuous reduction in RhB concentration due to dye adsorption.

As illustrated in Fig. 7(a–d), kinetic studies were performed using both pseudo-first-order and pseudo-second-order models. For OVS-DDSQ POIP, the pseudo-first-order model exhibited an excellent fit with a coefficient (R^2) of 0.9964, compared to an R^2 of 0.8161 for the

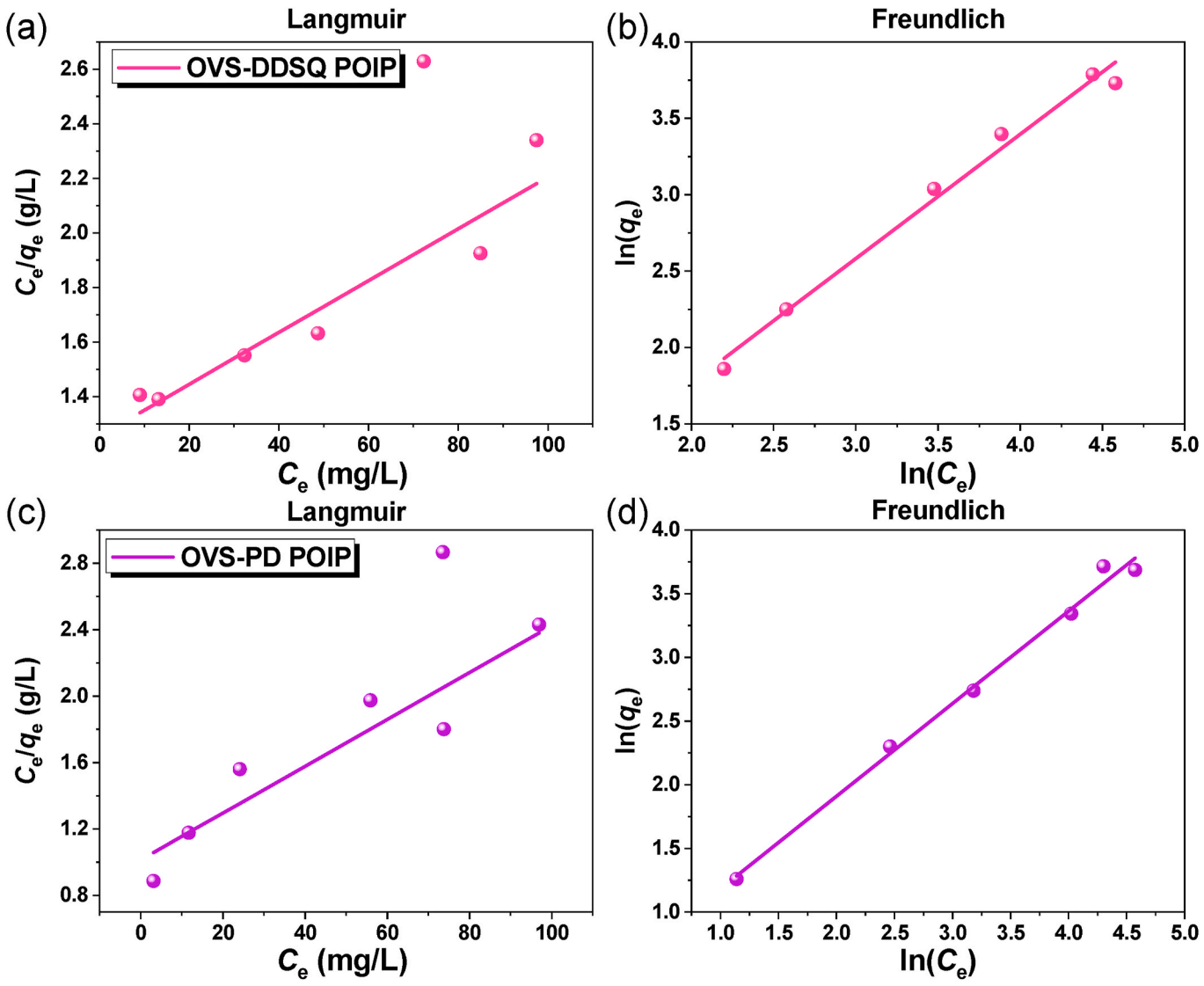

Fig. 8. Langmuir fitting for (a) OVS-PD POIP and (c) OVS-DDSQ POIP. Freundlich fitting for (b) OVS-PD POIP and (d) OVS-DDSQ POIP.

pseudo-second-order model, providing evidence that its adsorption behavior is more consistent with a pseudo-first-order process. In contrast, for OVS-PD POIP, the fitting coefficients were very similar for both models ($R^2 = 0.9934$ for pseudo-first-order and 0.9931 for pseudo-second-order). The pseudo-first-order rate constant ($|k_1|$) was determined to be 0.0145 min^{-1} for OVS-DDSQ POIP and 0.0008 min^{-1} for OVS-PD POIP, suggesting that OVS-DDSQ POIP exhibits superior physical adsorptions. Similarly, the pseudo-second-order rate constant (k_2) was 0.0031 g mg^{-1} min^{-1} for OVS-DDSQ POIP and 0.00027 g mg^{-1} min^{-1} for OVS-PD POIP, indicating enhanced chemisorption capability in OVS-DDSQ POIP. These kinetic parameters are outlined in Tables S1 and S2. The superior performance of OVS-DDSQ POIP adsorbents over OVS-PD POIP can be attributed to their enhanced surface area, which facilitates deeper penetration of dye molecules into the pore channels, thereby promoting more efficient chemisorption. Moreover, the rich phenyl content in the DDSQ structure enhances π–π interactions with dye molecules, further boosting the chemisorption process. This evidence suggests that chemisorption plays a dominant role in the adsorption mechanism, leading to rapid and efficient dye removal, as illustrated in Fig. 6(c).

Fig. S4 shows that RhB adsorption was conducted at various dye concentrations, and as the RhB concentration increased, the intensity of the remaining dye also increased. Notably, in solutions with excess RhB, OVS-DDSQ POIP exhibited much lower residual intensity compared to OVS-PD POIP, indicating its superior adsorption capability. A saturation curve was then plotted to determine the maximum adsorption capacity (q_{max}), as summarized in Fig. S5 and Table S3. OVS-DDSQ POIP demonstrated a higher saturation adsorption capacity than OVS-PD POIP. The fitting coefficients (R^2) for the Langmuir models were 0.9167 for OVS-DDSQ POIP and 0.8914 for OVS-PD POIP [Fig. 8(a) and (c)], while the Freundlich model yielded R^2 values of 0.9879 and 0.9930 for OVS-DDSQ POIP and OVS-PD POIP, respectively [Fig. 8(b) and (d)]. These high fitting coefficients indicate that both models describe the adsorption behavior well; However, the Freundlich model's more accurate representation points to a heterogeneous nature of the adsorption process. In cases where the Langmuir model provides a better fit, it hints that the adsorption sites are more homogeneous, which is typically observed in adsorbents with well-structured surfaces that facilitate chemisorption through functionalized units. A comparative analysis of the surface area and adsorption capacity of OVS-PD POIP and OVS-DDSQ PPIP toward RhB was performed with other reported adsorbent materials [Table S4]. The results indicate that both OVS-PD and OVS-DDSQ POIPs possess markedly higher BET surface areas and superior adsorption capacities, underscoring their strong potential as highly efficient and advanced adsorbent materials for dye removal applications. To further assess the practical applicability of these materials, the

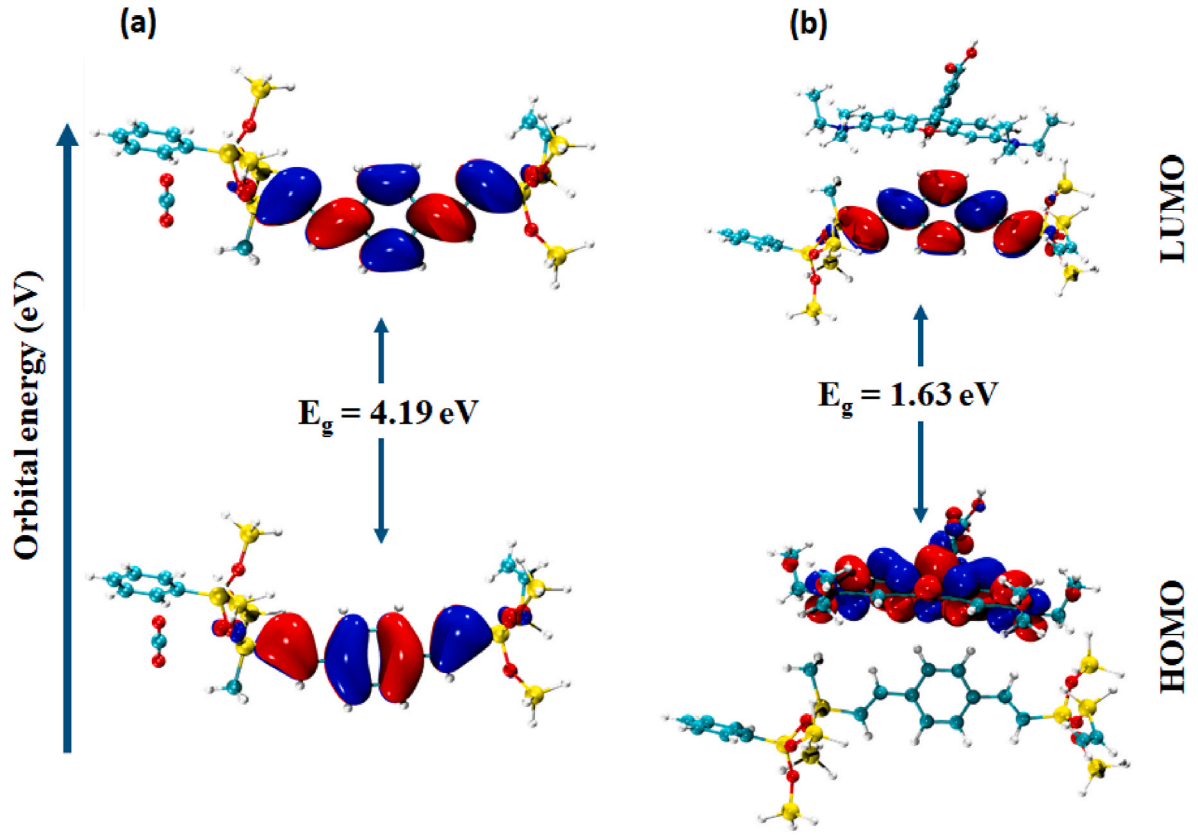

Fig. 9. The HOMO-LUMO orbitals for (a) CO_2-OVS-DDSQ POIP and (b) RhB-OVS-DDSQ POIP.

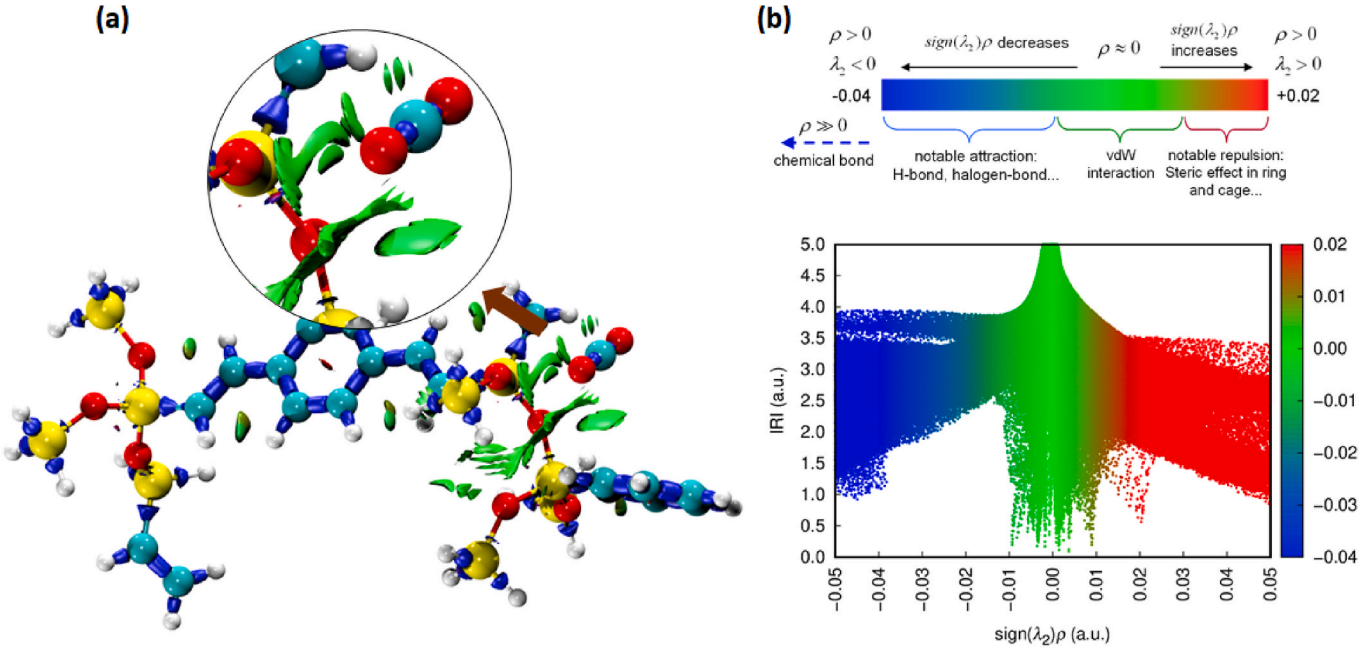

Fig. 10. The 3D isosurfaces (a) and 2D scatter map (b) of the CO_2-OVS-DDSQ POIP complex.

RhB adsorption performance of OVS-PD and OVS-DDSQ POIPs was investigated in simulated industrial wastewater. Compared with their performance under standard conditions, a pronounced reduction in removal efficiency was observed, with OVS-DDSQ POIP achieving only 29.6 % removal and OVS-PD POIP just 18.2 %. This significant decline is most likely due to the complex nature of the wastewater matrix, where a variety of coexisting ions and organic molecules compete with RhB for active sites or interact with the adsorbent through multiple intermolecular forces. Such competitive interactions weaken the affinity of the OVS-based POIPs toward RhB, leading to the observed decrease in adsorption efficiency, as shown in Fig. S6. The stability of the OVS-based POIPs was evaluated by immersing the materials in RhB solution for 24 h

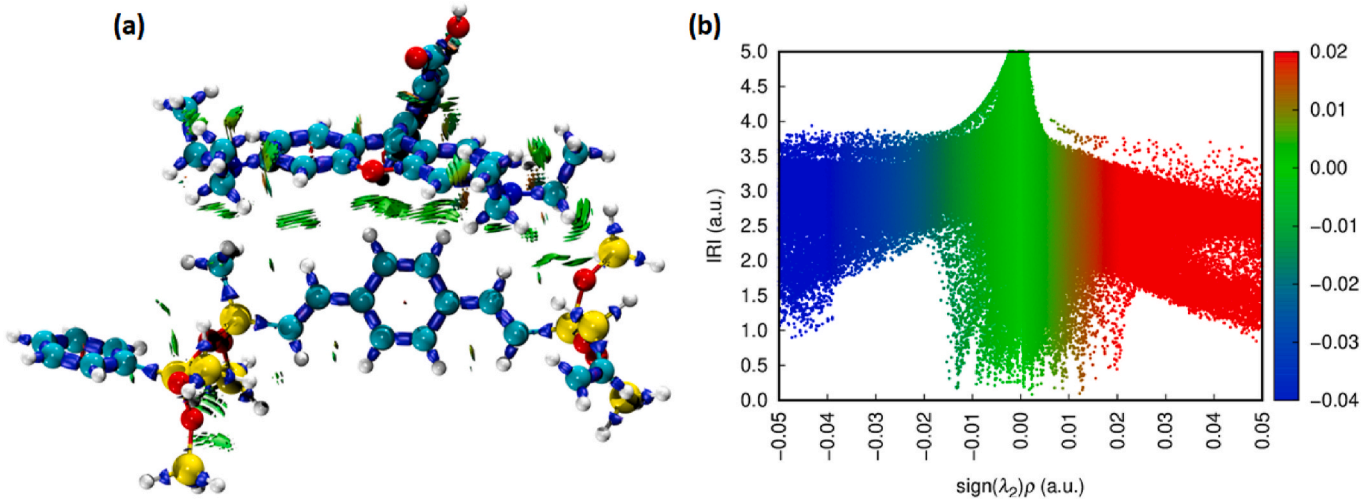

Fig. 11. The 3D isosurfaces (a) and 2D scatter map (b) of the RhB-OVS-DDSQ POIP complex.

[Figs. S7 and S8]. The FT-IR spectra after exposure showed new C═O stretching bands around 1740 cm^{-1} and noticeable broadening in the Si-O-Si region of OVS-DDSQ POIP and OVS-PD POIP, indicating strong interactions between the Si-O-Si cages and RhB. After dye removal and recovery through washing and drying, the FT-IR spectra of the treated POIPs closely resembled those of the pristine POIP materials, confirming that the structural integrity of the POIPs was fully preserved.

The molecular electrostatic potential (MESP) provides a visual representation of electronic density distribution within the molecule, enabling identification of potential binding sites. As illustrated in Fig. S9, the MESP map of the designed OVS-DDSQ POIP shows distinct regions: neutral potential (green), electron-rich with high negative potential (red), and electron-deficient with positive potential (blue). Such spatial variations in surface potential promote selective interactions with charged species, allowing recognition of both cations and anions. For CO_2, the electron-deficient carbon atom preferentially interacts with the electron-rich (red) regions of the OVS-DDSQ POIP. In contrast, its electron-rich oxygen atoms align with the electron-deficient (blue) regions. The red regions around the aromatic core and peripheral groups of the OVS-DDSQ POIP can further facilitate π-π interactions with the CO_2 carbon center, whereas the blue areas near hydrogen atoms may form hydrogen bonds with the CO_2 oxygen atoms. Together, these complementary interactions indicate that the OVS-DDSQ POIP offers multiple binding sites for effective CO_2 capture. In the case of RhB dye, the presence of heteroatoms provides several potential interaction sites. The OVS-DDSQ POIP surface, with its varied electrostatic potential regions, enables diverse binding modes with RhB. In particular, the electrophilic portion of RhB tends to orient toward the aromatic core of the OVS-DDSQ POIP, promoting stronger overlap and enhanced interactions. The highest occupied molecular orbital (HOMO) reflects a molecule's electron-donating ability, whereas the lowest unoccupied molecular orbital (LUMO) indicates its electron-accepting capacity. The energy gap between these orbitals (ΔE) is a key parameter for assessing molecular stability and electronic conductivity. Fig. 9 illustrates the HOMO and LUMO distributions of the CO_2-OVS-DDSQ POIP and RhB-OVS-DDSQ POIP complexes. For CO_2-OVS-DDSQ POIP, the calculated band gap of 4.19 eV suggests moderate electronic transitions, favoring physical adsorption of CO_2 on the OVS-DDSQ POIP surface. Such physisorption is advantageous, as it preserves the structural integrity of the catalyst for regeneration [Fig. 9(a)]. The HOMO in CO_2-OVS-DDSQ POIP is delocalized across the central aromatic core, indicating uniform electron cloud distribution, which supports efficient interaction. By contrast, the RhB-OVS-DDSQ POIP complex shows a much smaller band gap of 1.63 eV, signifying strong electronic charge transfer from the RhB dye to the OVS-DDSQ POIP framework [Fig. 9(b)]. This is supported by the orbital distribution: the HOMO is entirely localized on the dye, while the LUMO is confined to the OVS-DDSQ POIP. As a result, RhB adsorption redistributes electron density across the framework, driven by the dye's high intrinsic electron density, which enhances orbital overlapping and strengthens interaction with the OVS-DDSQ POIP surface.

3.4. Interaction region indicator (IRI)Analysis

Understanding non-covalent interactions is essential for elucidating adsorption mechanisms. The Independent Gradient Model based on Hirshfeld partitioning (IRI) provides a powerful graphical tool to visualize both covalent bonds and weaker intermolecular forces, thereby offering comprehensive insights into the interaction landscape. To analyze these interactions, two-dimensional (2D) reduced density gradient (RDG) plots versus λ_2 values, along with three-dimensional (3D) isosurfaces, were generated for CO_2-OVS-DDSQ POIP and RhB-OVS-DDSQ POIP complexes [Figs. 10 and 11]. In the CO_2-OVS-DDSQ POIP system, well-defined green isosurfaces appear between the polymeric framework and the CO_2 molecule, clearly indicating non-covalent interactions originating from the silicon, oxygen, and aromatic domains of the OVS-DDSQ POIP [Fig. 10(a)]. Specifically, the oxygen atoms of CO_2 engage in interactions with Si-O groups of the OVS-DDSQ POIP, while additional C-O and C-C contacts are established with the delocalized π-electron cloud of the aromatic core. These cooperative interactions contribute to electrostatic stabilization, in agreement with the trends predicted by HOMO-LUMO orbital analysis. The corresponding RDG scatter plot [Fig. 10(b)] corroborates these observations, displaying characteristic peaks in the 0.0 to −0.01 range, which are typical signatures of weak non-covalent forces.

For the RhB-OVS-DDSQ POIP complex, the 3D isosurfaces and corresponding 2D RDG scatter plots are shown in Fig. 11. The 3D visualization [Fig. 11(a)] displays weak, discontinuous interaction between RhB and the OVS-DDSQ POIP surface, characteristic of van der Waals forces. In contrast, the 2D scatter plot reveals distinct spikes in the range of $\lambda_2 = 0$ to −0.15 a. u., with notable intensity between −0.01 and −0.15 a. u., confirming the presence of significant non-covalent interactions [Fig. 11(b)]. Overall, both CO_2 and RhB exhibit favorable adsorption onto the OVS-DDSQ POIP, consistent with experimental results.

4. Conclusion

We have successfully synthesized DDSQ-Br monomer and integrated it into OVS-based POIPs via distinct synthetic routes. Comprehensive spectroscopic analyses confirmed that the Grubbs reaction yields well-

defined monomeric units, whereas the Heck reaction promotes the formation of DDSQ oligomers. The resulting OVS-based POIPs display hierarchical pore structures with high specific surface areas and excellent thermal stability, attributes that are critical for efficient gas and dye adsorption. CO_2 uptake measurements clearly indicate that the OVS-DDSQ POIP outperforms the OVS-PD POIP, likely due to enhanced polar-π interactions provided by the DDSQ structure. Furthermore, RhB adsorption studies demonstrate rapid and efficient dye removal, with kinetic analyses favoring a pseudo-first-order model for OVS-DDSQ POIP. Overall, these findings highlight the potential of OVS-based POIPs as multifunctional materials for environmental remediation, capable of addressing challenges in both CO_2 capture and pollutant dye removal.

CRediT authorship contribution statement

Yang-Chin Kao: Writing – original draft, Formal analysis, Data curation, Conceptualization. **Pin-Han Chen:** Formal analysis, Data curation, Conceptualization. **Cheng-Yu Chen:** Investigation, Formal analysis, Data curation, Conceptualization. **Hui-Wen Chen:** Formal analysis. **Wei-Cheng Chen:** Formal analysis. **Mohsin Ejaz:** Formal analysis. **Mohammed G. Kotp:** Data curation. **Mohamed Gamal Mohamed:** Supervision, Investigation, Formal analysis, Data curation, Conceptualization. **Hira Karim:** Software. **Shiao-Wei Kuo:** Supervision, Resources, Project administration.

Declaration of competing interest

The authors declare that they have no known competing financial interests or personal relationships that could have appeared to influence the work reported in this paper.

Acknowledgments

This study was supported financially by the National Science and Technology Council, Taiwan, under contracts NSTC 113-2223-E-110-001- and 113-2221-E-110-012-MY3. The authors thank the staff at National Sun Yat-sen University for their assistance with the TEM (ID: EM022600) experiments.

Appendix A. Supplementary data

Supplementary data to this article can be found online at https://doi.org/10.1016/j.polymer.2025.129041.

Data availability

Data will be made available on request.

References

[1] V.V. Chandanshive, S.K. Kadam, R.V. Khandare, M.B. Kurade, B.H. Jeon, J. P. Jadhav, S.P. Govindwar, In situ phytoremediation of dyes from textile wastewater using garden ornamental plants, effect on soil quality and plant growth, Chemosphere 210 (2018) 968–976, https://doi.org/10.1016/j.CMSHAF.2018.07.064.

[2] X.X. Wang, L. Chen, L. Wang, Q. Fan, D. Pan, J. Li, F. Chi, Y. Xie, S. Yu, C. Xiao, F. Luo, J. Wang, X. Wang, C. Chen, W. Wu, W. Shi, S. Wang, X. Wan, Synthesis of novel nanomaterials and their application in efficient removal of radionuclides, Sci. China Chem. 62 (2019) 933–967, https://doi.org/10.1007/s11426-019-9492-4.

[3] Y. Zhang, X. Hong, C.M. Cao, X.Q. Huang, B. Hu, S.Y. Ding, H. Lin, Functional porous organic polymers with conjugated triaryl triazine as the core for superfast adsorption removal of organic dyes, ACS Appl. Mater. Interfaces 13 (2021) 6359–6366, https://doi.org/10.1021/acsami.0c21374.

[4] J. Tang, R. Xu, G. Sui, D. Guo, Z. Zhao, S. Fu, X. Yang, Y. Li, J. Li, Double-shelled porous g-C_3N_4 nanotubes modified with amorphous Cu-Doped FeOOH nanoclusters as 0D/3D non-homogeneous photo-fenton catalysts for effective removal of organic dyes, Small 19 (2023) 2208232, https://doi.org/10.1002/smll.202208232.

[5] C.W. Hsiao, A.M. Elewa, M.G. Mohamed, S.W. Kuo, Highly stable hybrid porous polymers containing polyhedral oligomeric silsesquioxane (POSS)/dibenzo[g,p] chrysene and dibenzo[b,d]thiophene units for efficient rhodamine B dye removal, Sep. Purif. Technol. 332 (2024) 125771, https://doi.org/10.1016/j.seppur.2023.125771.

[6] Y.C. Kao, K.T. Yeh, M.G. Mohamed, H. Karim, W.H. Su, S.W. Kuo, Structural modulation via mesoporous silica templating in covalent organic frameworks: converting functional aspects for adsorption behavior, Sep. Purif. Technol. 375 (2025) 133827, https://doi.org/10.1016/j.seppur.2025.133827.

[7] E. Sivasurya, R. Atchudan, M.G. Mohamed, A. Thangamani, S. Rajendran, A. Jalil, P.K. Kalambate, D. Manoj, S.W. Kuo, Electrocatalytic conversion of CO_2 into selective carbonaceous fuels using metal-organic frameworks: an overview of recent progress and perspectives, Mater. Today Chem. 44 (2025) 102538, https://doi.org/10.1016/j.mtchem.2025.102538.

[8] M.G. Mohamed, C.C. Chen, M. Ibrahim, A.O. Mousa, M.H. Elsayed, Y. Ye, S.W. Kuo, Tetraphenylanthraquinone and dihydroxybenzene-tethered conjugated microporous polymer for enhanced CO_2 uptake and supercapacitive energy storage, JACS Au 4 (2024) 3593–3605, https://doi.org/10.1021/jacsau.4c00537.

[9] W. Gong, Q. Wu, L. Ma, W. Zhang, X. Li, A. Xu, S. Zhao, MnOx/g-C_3N_4 nanocomposites mediated sulfite activation for enhanced organic pollutants degradation under visible light irradiation, Colloids Surf., A: Physicochem. Eng. 659 (2023) 130812, https://doi.org/10.1016/j.colsurfa.2022.130812.

[10] A.R. Ghadim, S. Dadkhah, M. Abdouss, A. Khataee, S. Sattari, M. Fattahi, Development of a novel Z-scheme CoxNi1−xTiO$_3$/CdS (X = 0.5) photocatalyst for the efficient degradation of organic pollutants via a visible-light-driven photocatalytic process, J. Colloid Sci. 663 (2024) 1035–1051, https://doi.org/10.1016/j.jcis.2024.03.005.

[11] X. Zhang, S. Li, Y. Wang, J. Shen, Y. Wei, C. Wang, Preparation of amino/hydroxy dual-functionalized hypercrosslinked polymers for effective removal of organic dyes from water, J. Hazard. Mater. 488 (2025) 137405, https://doi.org/10.1016/j.jhazmat.2025.137405.

[12] B. Qiu, Q. Shao, J. Shi, C. Yang, H. Chu, Application of biochar for the adsorption of organic pollutants from wastewater: modification strategies, mechanisms and challenges, Sep. Purif. Technol. 300 (2022) 121925, https://doi.org/10.1016/j.seppur.2022.121925.

[13] K. Zhu, C. Liu, W. Xia, Y. Wang, H. He, L. Lei, Y. Ai, W. Chen, X. Liu, Non-radical pathway dominated degradation of organic pollutants by nitrogen-doped microtube porous graphitic carbon derived from biomass for activating peroxymonosulfate: performance, mechanism and environmental application, J. Colloid Sci. 625 (2022) 890–902, https://doi.org/10.1016/j.jcis.2022.06.078.

[14] X. Zhang, M. Kamali, T. Uleners, J. Symus, S. Zhang, Z. Liu, M.E.V. Costa, L. Appels, D. Cabooter, R. Dewil, UV/TiO_2/periodate system for the degradation of organic pollutants – Kinetics, mechanisms and toxicity study, Chem. Eng. J. 449 (2022) 137680, https://doi.org/10.1016/j.cej.2022.137680.

[15] V. Dutta, S. Sonu, P. Raizada, V.K. Thakur, T. Ahamad, S. Thakur, P.K. Verma, H.H. P. Quang, V.H. Nguyen, P. Singh, Prism-like integrated Bi_2WO_6 with Ag-$CuBi_2O_4$ on carbon nanotubes (CNTs) as an efficient and robust S-scheme interfacial charge transfer photocatalyst for the removal of organic pollutants from wastewater, Environ. Sci. Pollut. Res. 30 (2023) 124530–124545, https://doi.org/10.1007/s11356-022-20743-8.

[16] Q. Zheng, H. Zhang, J. Li, X. Yu, X. Gao, Z. Wang, Amino acid assisted-construction of 2D-hierarchical MFI zeolites for adsorption of rhodamine B, Sep. Purif. Technol. 358 (2025) 130414, https://doi.org/10.1016/j.seppur.2024.130414.

[17] A.A. Al-Gheethi, Q.M. Azhar, P.S. Kumar, A.A. Yusuf, A.K. Al-Buriahi, R.M.S. R. Mohamed, M.M. Al-shaibani, Sustainable approaches for removing rhodamine B dye using agricultural waste adsorbents: a review, Chemosphere 287 (2022) 132080, https://doi.org/10.1016/j.CMSHAF.2021.132080.

[18] K. Naseem, E. Abrar, A. Khalid, M.A. Ismail, Inorganic nanoparticles as a potential catalyst for the reduction of rhodamine B dye: a critical review, Inorg. Chem. Commun. 163 (2024) 112367, https://doi.org/10.1016/j.inoche.2024.112367.

[19] Z.M. Saigl, Various adsorbents for removal of rhodamine b dye: a review, Indones. J. Chem. 21 (2021) 1039–1056, https://doi.org/10.22146/ijc.62863.

[20] S. Jiang, Y. Lyu, J. Zhang, X. Zhang, M. Yuan, Z. Zhang, G. Jin, B. He, W. Xiong, H. Yi, Continuous adsorption removal of organic pollutants from wastewater in a UiO-66 fixed bed column, J. Environ. Chem. Eng. 12 (2024) 111951, https://doi.org/10.1016/j.jece.2024.111951.

[21] Q.Y. Yang, X.J. Gao, G.D. Qi, Y. Wang, W.W. Dong, Z.F. Tian, J. Zhao, D.S. Li, Q. Zhang, Dye-anchoring strategy with a metal–organic framework for a highly efficient visible-light-driven photocatalytic CO_2 reduction through the solid–gas mode, ACS Appl. Energy Mater. 6 (2023) 334–341, https://doi.org/10.1021/acsaem.2c03123.

[22] S. Gazvineh, S. Beyranvand, S. Saki, M. Nemati, K. Ludwig, P. Amsalem, T. Schultz, C. Cheng, M. Adeli, Thermoresponsive scaffolds fabricated using covalent organic frameworks for the selective removal of water contaminants, Mater. Adv. 5 (2024) 9673–9683, https://doi.org/10.1039/D4MA00792A.

[23] Z. Chen, Y. Li, Y. Cai, S. Wang, B. Hu, B. Li, X. Ding, L. Zhuang, X. Wang, Application of covalent organic frameworks and metal–organic frameworks nanomaterials in organic/inorganic pollutants removal from solutions through sorption-catalysis strategies, Carbon Res. 2 (2023) 8, https://doi.org/10.1007/s44246-023-00041-9.

[24] H. Zhou, Q. Ye, J. Xu, Polyhedral oligomeric silsesquioxane-based hybrid materials and their applications, Mater. Chem. Front. 1 (2017) 212–230, https://doi.org/10.1039/C6QM00062B.

[25] W. Yu, J. Fu, X. Dong, L. Chen, L. Shi, A graphene hybrid material functionalized with POSS: synthesis and applications in low-dielectric epoxy composites, Compos.

Sci. Technol. 92 (2014) 112–119, https://doi.org/10.1016/j.compscitech.2013.12.016.
[26] M.G. Mohamed, S.W. Kuo, Progress in the self-assembly of organic/inorganic polyhedral oligomeric silsesquioxane (POSS) hybrids, Soft Matter 18 (2022) 5535–5561, https://doi.org/10.1039/D2SM00635A.
[27] J. Ozimek, K. Pielichowski, Recent advances in Polyurethane/POSS hybrids for biomedical applications, Molecules 27 (2021) 40, https://doi.org/10.3390/molecules27010040.
[28] J. Ozimek, I. Łukaszewska, K. Pielichowski, POSS and SSQ materials in dental applications: recent advances and future outlooks, Int. J. Mol. Sci. 24 (2023) 4493, https://doi.org/10.3390/ijms24054493.
[29] S. Liu, R. Guo, C. Li, C. Lu, G. Yang, F. Wang, J. Nie, C. Ma, M. Gao, POSS hybrid hydrogels: a brief review of synthesis, properties and applications, Eur. Polym. J. 143 (2021) 110180, https://doi.org/10.1016/j.eurpolymj.2020.110180.
[30] C.Y. Chen, W.C. Chen, M.G. Mohamed, Z.Y. Chen, S.W. Kuo, Highly thermally stable, reversible, and flexible main chain type benzoxazine hybrid incorporating both polydimethylsiloxane and double-decker shaped polyhedral silsesquioxane units through diels–alder reaction, Macromol. Rapid Commun. 44 (2023) 2200910, https://doi.org/10.1002/marc.202200910.
[31] M.G. Mohamed, N.Y. Liu, A.F.M. EL-Mahdy, S.W. Kuo, Ultrastable luminescent hybrid microporous polymers based on polyhedral oligomeric silsesquioxane for CO_2 uptake and metal ion sensing, Microporous Mesoporous Mater. 311 (2021) 110695, https://doi.org/10.1016/j.micromeso.2020.110695.
[32] Y.T. Liao, Y.C. Lin, S.W. Kuo, Highly thermally stable, transparent, and flexible polybenzoxazine nanocomposites by combination of double-decker-shaped polyhedral silsesquioxanes and polydimethylsiloxane, Macromolecules 50 (2017) 5739–5747, https://doi.org/10.1021/acs.macromol.7b01085.
[33] M.G. Mohamed, M.H.A.E. Hassan, A. Basit, I.M.A. Mekhemer, H.H. Chou, K. H. Chen, S.W. Kuo, Hybrid porous polymers combination of octavinylsilsesquioxane/pyrene with benzothiadiazole units for robust energy storage and efficient photocatalytic hydrogen production from water, ACS Appl. Polym. Mater. 6 (2024) 5945–5956, https://doi.org/10.1021/acsapm.4c00655.
[34] S. Xia, Y. Yang, W. Zhu, C. Lü, Quaternized polyhedral oligomeric silsesquioxanes stabilized Pd nanoparticles as efficient nanocatalysts for reduction reaction, Colloids Surf., A: Physicochem. Eng. 585 (2020) 124110, https://doi.org/10.1016/j.colsurfa.2019.124110.
[35] S. Zhang, F. Zhang, M. Yang, P. Fang, POSS modified NixOy-decorated TiO_2 nanosheets: nanocomposites for adsorption and photocatalysis, Appl. Surf. Sci. 566 (2021) 150604, https://doi.org/10.1016/j.apsusc.2021.150604.
[36] C.W. Hsiao, A.M. Elewa, M.G. Mohamed, M.G. Kotp, M.M.C. Chou, S.W. Kuo, Designing strategically functionalized hybrid porous polymers with octavinylsilsesquioxane/dibenzo[g,p]chrysene/benzo[c]-1,2,5-thiadiazole units for rapid removal of rhodamine B dye from water, Colloids Surf., A: Physicochem. Eng. 699 (2024) 134658, https://doi.org/10.1016/j.colsurfa.2024.134658.
[37] Q. Meng, L. Yu, X. Yang, R. Gao, H. Chang, Y. Wu, Z. Yang, A. Xu, S. Gao, F. Liu, Synthesis of hypercross-linked hybrid polyanilines from hollow spherical polyaniline and octavinylsilsesquioxane and its dye adsorption performance, Mater. Today Commun. 34 (2023) 105488, https://doi.org/10.1016/j.mtcomm.2023.105488.
[38] S. Hussain, R. Kunthom, H. Liu, Hybrid dendrimer network based on silsesquioxane and glycidyl methacrylate for enhanced adsorption of iodine and dyes in environmental remediation, Chem. Asian J. 19 (2024) e202400584, https://doi.org/10.1002/asia.202400584.
[39] M. Ejaz, M.G. Mohamed, W.C. Huang, Y.C. Kao, W.C. Chen, S.W. Kuo, Highly thermally stable polyhedral oligomeric silsesquioxane based on diacetal-functionalized polybenzoxazine nanocomposites, Eur. Polym. J. 223 (2025) 113649, https://doi.org/10.1016/j.eurpolymj.2024.113649.
[40] T.C. Chou, S.W. Kuo, Controllable wet-brush blending of linear diblock copolymers with Phenolic/DDSQ hybrids toward mesoporous structure phase diagram, Macromolecules 75 (2024) 5958–5970, https://doi.org/10.1021/acs.macromol.4c00665.
[41] S.W. Kuo, F.C. Chang, POSS related polymer nanocomposites, Prog. Polym. Sci. 36 (2011) 1649–1696, https://doi.org/10.1016/j.progpolymsci.2011.05.002.
[42] T. Hamada, S. Takase, A. Tanaka, K. Okada, S. Mineoi, A. Uedono, J. Ohshita, Double-decker silsesquioxane-grafted polysilsesquioxane hybrid films as thermal insulation materials, ACS Appl. Polym. Mater. 5 (2023) 743–750, https://doi.org/10.1021/acsapm.2c01743.
[43] C.Y. Chen, M.G. Mohamed, W.C. Chen, S.W. Kuo, Construction of ultrastable porous carbons materials derived from organic/inorganic double decker silsesquioxane (DDSQ) hybrid as a high-performance electrode for supercapacitor, Mater. Today Chem. 34 (2023) 101773, https://doi.org/10.1016/j.mtchem.2023.101773.
[44] Z.Y. Chen, W.C. Chen, S.W. Kuo, Enhanced thermal and porous properties of double-decker-shaped polyhedral silsesquioxane-bismaleimide (DDSQ-BMI) nanocomposites for high-performance CO_2 storage and supercapacitors, Polym. Chem. 15 (2024) 53–564, https://doi.org/10.1039/D3PY01115A.
[45] X. Lin, Y.Y. Deng, Q. Zhang, D. Han, Q. Fu, Effect of POSS size on the porosity and adsorption performance of hybrid porous polymers, Macromolecules 56 (2023) 1243–1252, https://doi.org/10.1021/acs.macromol.2c02486.
[46] L. Miao, L. Zhan, S. Liao, Y. Li, T. He, S. Yin, L. Wu, H. Qiu, The recent advances of Polymer–POSS nanocomposites with low dielectric constant, Macromol. Rapid Commun. 45 (2024) 2300601, https://doi.org/10.1002/marc.202300601.
[47] L. Fan, X. Wang, D. Wu, Polyhedral oligomeric silsesquioxanes (POSS)-Based hybrid materials: molecular design, solution self-assembly and biomedical applications, Chin. J. Chem. 39 (2021) 757–774, https://doi.org/10.1002/cjoc.202000536.
[48] K. Mituła, R. Januszewski, J. Duszczak, M. Rzonsowska, B. Dudziec, High thermally stable polysiloxanes cross-linked with di(alkenyl)functionalized DDSQs exhibiting swelling abilities, Eur. Polym. J. 171 (2022) 111191, https://doi.org/10.1016/j.eurpolymj.2022.111191.
[49] H. Yonezawa, K. Naka, H. Imoto, Open and closed cage silsesquioxane dimers, ChemPlusChem 89 (2024) e202400301, https://doi.org/10.1002/cplu.202400301.
[50] Q. Wang, M. Unno, H. Liu Silsesquioxane-Based, Triphenylamine-linked fluorescent porous polymer for dyes adsorption and nitro-aromatics detection, Materials 14 (2021) 3851, https://doi.org/10.3390/ma14143851.
[51] W.C. Chen, Z.Y. Chen, Y. Ba, B. Wang, G. Chen, X. Fang, S.W. Kuo, Double-decker-shaped polyhedral silsesquioxanes reinforced epoxy/bismaleimide hybrids featuring high thermal stability, Polymers 14 (2022) 2380, https://doi.org/10.3390/polym14122380.
[52] H. Wang, G. Hang, J. Hu, Y. Gao, L. Li, S. Zheng, Organic–inorganic polyimides with POSS cages in the main chains: an impact of POSS R groups on morphologies and properties, ACS Appl. Polym. Mater. 5 (2023) 4274–4287, https://doi.org/10.1021/acsapm.3c00456.
[53] M.G. Mohamed, T.H. Mansoure, Y. Takashi, M.M. Samy, T. Chen, S.W. Kuo, Ultrastable porous organic/inorganic polymers based on polyhedral oligomeric silsesquioxane (POSS) hybrids exhibiting high performance for thermal property and energy storage, Microporous Mesoporous Mater. 328 (2021) 111505, https://doi.org/10.1016/j.micromeso.2021.111505.
[54] W.J. Wang, K.H. Chen, Z.W. Yang, B.W. Peng, L.N. He, Tuning of visible light-driven CO_2 reduction and hydrogen evolution activity by using POSS-Modified porous organometallic polymers, J. Mater. Chem. A 9 (2021) 16699–16705, https://doi.org/10.1039/D1TA04418D.
[55] L. Li, H. Wang, S. Zheng, Well-defined difunctional POSS macromers and related organic–inorganic polymers: precision synthesis, structure and properties, J. Polym. Sci. 62 (2024) 583–613, https://doi.org/10.1002/pol.20230428.
[56] A. Magne, E. Carretier, L.U. Ruiz, T. Clair, M. Le Hir, P. Moulin, Recovery of homogeneous platinoid catalysts from pharmaceutical media: review on the existing treatments and the perspectives of membrane processes, Membranes 13 (2023) 738, https://doi.org/10.3390/membranes13080738.
[57] S.G. Patra, N.K. Das, Recent advancement on the mechanism of olefin metathesis by grubbs catalysts: a computational perspective, Polyhedron 200 (2021) 115096, https://doi.org/10.1016/j.poly.2021.115096.
[58] M.R. Swart, L. Twigge, E. Erasmus, C. Marais, B.C.B. Bezuidenhoudt, Olefin metathesis, p-Cresol, and the second generation grubbs catalyst: fitting the pieces, Eur. J. Inorg. Chem. 2021 (2021) 1752–1762, https://doi.org/10.1002/ejic.202100078.
[59] M.R. Swart, C. Marais, E. Erasmus, Comparison of the spectroscopically measured catalyst transformation and electrochemical properties of grubbs' First- and second-generation catalysts, ACS Omega 6 (2021) 28642–28653, https://doi.org/10.1021/acsomega.1c03109.
[60] W.C. Chen, S.W. Kuo, Ortho-imide and allyl groups effect on highly thermally stable polybenzoxazine/double-decker-shaped polyhedral silsesquioxane hybrids, Macromolecules 51 (2018) 9602–9612, https://doi.org/10.1021/acs.macromol.8b02207.
[61] W.C. Chen, Y.T. Liu, S.W. Kuo, Highly thermal stable phenolic resin based on double-decker-shaped POSS nanocomposites for supercapacitors, Polymers 12 (2020) 2151, https://doi.org/10.3390/polym12092151.
[62] H.W. Chen, M.G. Mohamed, Y.C. Kao, W.C. Chen, K. Chiou, S.W. Kuo, Overcoming synthetic challenges in developing high-performance polybenzoxazine from diamine-functionalized double-decker silsesquioxane (DDSQ) cage, Eur. Polym. J. 232 (2025) 113929, https://doi.org/10.1016/j.eurpolymj.2025.113929.
[63] P.M. Zelisko, K.K. Flora, J.D. Brennan, M.A. Brook, Water-in-silicone oil emulsion stabilizing surfactants formed from native albumin and α,ω-triethoxysilylpropyl-polydimethylsiloxane, Biomacromolecules 9 (2008) 2153–2161, https://doi.org/10.1021/bm800226z.